AGU100 ADVANCING EARTH AND SPACE SCIENCE

Water Resources Research

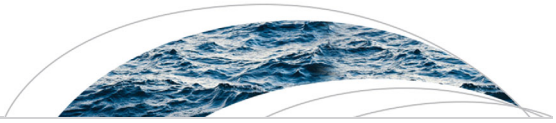

RESEARCH ARTICLE
10.1029/2017WR021533

Modeling Sedimentation Dynamics of Sediment-Laden River Intrusions in a Rotationally-Influenced, Stratified Lake

Kara R. Scheu[1,2], Derek Fong[1], Stephen G. Monismith[1], and Oliver B. Fringer[1]

[1]Department of Civil and Environmental Engineering, Stanford University, Stanford, CA, USA, [2]Integral Consulting Inc., Portland, OR, USA

Key Points:
- A validated three-dimensional hydrodynamic and sediment transport model was shown to accurately reproduce complex intrusion dynamics
- The ambient stratification of a lacustrine system impacts the intrusion speed and thickness and dictates the sedimentation extent
- A simple analytical expression was developed to predict sedimentation extent using only a priori knowledge of stratification and flow rate

Correspondence to:
K. R. Scheu,
karascheu@gmail.com

Citation:
Scheu, K. R., Fong, D., Monismith, S. G., & Fringer, O. B. (2018). Modeling sedimentation dynamics of sediment-laden river intrusions in a Rotationally-Influenced, Stratified Lake. *Water Resources Research*, *54*, 4084–4107. https://doi.org/10.1029/2017WR021533

Received 15 JUL 2017
Accepted 27 APR 2018
Accepted article online 7 MAY 2018
Published online 30 JUN 2018

Abstract River inflows are often the dominant source of sediment into a lacustrine system and the extent of sediment transport can be an important indicator of the impact of introduced constituents on an ecosystem. Inflow intrusions, which intrude into the middle of the water column at a depth of neutral buoyancy, can be common in deep, stratified lakes and reservoirs. However, the dynamics and associated sediment transport of these flows have received less attention in the literature compared to surface or underflow plumes. A three-dimensional hydrodynamic and sediment transport model was used to investigate sediment transport due to inflow intrusions in Pallanza Bay, an embayment within Lake Maggiore, Italy. The model was validated using field observations of inflow intrusions over varying conditions and was then used to simulate a range of realistic scenarios to evaluate sediment transport and deposition from inflow intrusions. The extent of sedimentation across the range of simulated scenarios can be estimated using a simple analytical expression with only a priori known parameters. The expression is a function of the intrusion plume speed and thickness, which are governed by the volume flow rate and the ambient stratification. We utilize the first-mode wave speed to characterize the ambient stratification in the simplified expression, which eliminates the need to characterize near-field mixing and entrainment to predict the intrusion depth. While the simple expression gives a reasonable estimate of the sedimentation extent, it does not capture lateral variability in the plume due to effects like lateral spreading and the earth's rotation.

1. Introduction

Suspended sediment and associated nutrients and contaminants can affect the ecological health and function of lakes and reservoirs. River inflows are often the dominant source of nutrients, sediments, and contaminants in a lacustrine system and the fate and transport of river-borne constituents depends in large part on the hydrodynamics of these inflows (Rueda & MacIntyre, 2010; Fischer & Smith, 1983). The form of an inflow plume is dictated by the river plume density relative to that of the ambient water body. A river inflow that is less dense than the ambient surface waters will propagate along the surface (e.g., coastal freshwater plumes or warm lacustrine inflows), while a river inflow that is more dense will plunge beneath the surface and propagate along the bottom as an underflow (e.g., turbidity currents or cold lacustrine inflows) (Ford & Johnson, 1983; Alavian et al., 1992; Rueda & MacIntyre, 2010). In a stratified water body, the dense plume may reach a depth of neutral buoyancy and will then intrude into the water column and form an inflow intrusion. Intrusions differ from surface or underflows because the plume moves through the water column at a depth of neutral buoyancy where the intrusion and the ambient buoyancy are similar (Ford & Johnson, 1983). Although intrusions are common in deep, stratified lacustrine systems (Cortés et al., 2014; Pilotti et al., 2014; Scheu et al., 2015; Fischer & Smith, 1983), the transport dynamics of intrusions have received significantly less attention in the literature compared to near-field mixing dynamics, surface plumes, and underflows. An important parameter in characterizing sediment transport and determining the impact of sediment and sediment-borne constituents on an ecosystem is the extent of sediment deposition, defined as the distance from the mouth at which sediment settles out of the water column (Geyer et al., 2004; Hill et al., 2000). Therefore, the main focus of this manuscript is to develop and evaluate an expression for the extent of sedimentation from river inflow intrusions into a stratified and rotational lacustrine system.

The dynamics of dense river plumes before the plumes intrude into the water column are supported by a large body of literature that includes analytical models, laboratory experiments, and numerical simulations

in simplified conditions. Upon entering a water body, a negatively buoyant river inflow will lose momentum due to widening and/or deepening of the plume cross-section, and will transition from a momentum-dominated plume to a density-driven current. At this point, the plume plunges beneath the lake surface and can entrain ambient water. The submerged plume then propagates along the bottom as an underflow, which can continue to entrain ambient water until it reaches a depth of neutral buoyancy (or sinks to the bottom). The amount of mixing and entrainment in the plunging and density current region of the plume are commonly parameterized as a function of the densimetric Froude number (Alavian et al., 1992; Cenedese & Adduce, 2010; Ellison & Turner, 1959; Ford & Johnson, 1983; Imberger & Hamblin, 1982; Turner, 1986) defined as $Fr=u_0(g_0'h_0)^{-1/2}$, where u_0 is the inflow velocity, h_0 is the river depth, and $g_0'=g\Delta\rho\rho_0^{-1}$ is the reduced gravity due to the density difference between the inflow and the ambient surface waters, $\Delta\rho$, relative to a reference density $\rho_0=1000$ kg m^{-3}. The near-field dynamics therefore dictate the amount of entrainment and the ultimate depth of the inflow intrusion in a stratified water body and this region has received significant attention in the literature (Cortés et al., 2014; Fischer et al., 1979; Wells & Nadarajah, 2009; Wells et al., 2010). The dynamics and sediment transport arising from inflow intrusions beyond the near-field mixing region have received limited attention in the literature.

Once a plume intrudes into the water column, the buoyancy-driven current is expected to propagate at a speed proportional to the internal wave speed, $c=(g'h)^{1/2}$, where h is the plume thickness and g' is the reduced gravity of the plume. For an inflow intrusion, the density difference driving the current is governed by the buoyancy frequency across the intrusion defined as $N^2=g\rho_0^{-1}\partial\rho/\partial z$ and approximated by $g'h_{int}$, where h_{int} is the intrusion thickness. The intrusion plume speed, u_{int}, is then given by

$$u_{int} \sim Nh_{int}, \tag{1}$$

where the coefficient of proportionality ranges from 0.2-0.5 in the literature (Benjamin, 1968; Bolster et al., 2008; Ford & Johnson, 1983; Imberger & Hamblin, 1982; Maxworthy et al., 2002; Nof & Gorder, 1988).

The intrusion thickness, h_{int}, is an important parameter in defining the intrusion plume speed, and errors in estimating the thickness will lead to errors in the estimated plume velocity (Ford & Johnson, 1983; Imberger & Hamblin, 1982). In a laterally confined system where the plume width (W) is equivalent to the width of the lake (B), the intrusion thickness is given by

$$h_{int} \approx \left(\frac{Q}{NW}\right)^{1/3}, \tag{2}$$

where Q is the volumetric flow rate (Fischer et al., 1979; Ford & Johnson, 1983; Imberger & Hamblin, 1982). While the vast majority of research on inflow intrusions beyond the near-field has been conducted in laterally confined riverine lakes where the width of the plume is constrained by the geometry of the lake ($W = B$) (Killworth & Carmack, 1979; Chikita, 1990; Chung et al., 2009; El-Gawad et al., 2012), the dynamics of the plume will differ for a laterally constrained plume compared to a laterally unconstrained plume. In a wide system in which the plume can spread laterally, Imberger and Hamblin (1982) suggest that the laterally unconstrained intrusion thickness can be approximated with

$$h_{int,lu} \approx (QN^{-1})^{1/3}, \tag{3}$$

such that the laterally unconstrained intrusion velocity is given by

$$u_{int,lu} \approx (QN^2)^{1/3}. \tag{4}$$

In a system large enough to be influenced by rotation of the earth, the trajectory of the plume will also be modified. The influence of rotation on the near-field river plume dynamics is governed by the ratio of the inertial radius of the inflow ($L_i=uf^{-1}$, where f is the Coriolis parameter) to the river mouth width (b). Depending on the inflow Rossby number (defined as $Ro_i=u_0(fb)^{-1}$) the inflow will follow the boundary upon leaving the river mouth ($Ro_i < 1$) or propagate into the ambient water body before feeling the influence of rotation ($Ro_i > 1$) (Fong & Geyer, 2002; Horner-Devine et al., 2006; Pimenta et al., 2011). For river plumes in lakes, typically $Ro_i > 1$ (with some exceptions), implying that inflow intrusions in lakes are deflected due to rotation after entering the lacustrine system. Far from the mouth, the Rossby radius of deformation ($L_R=u_df^{-1}$, where u_d is the appropriate density-driven plume speed) will govern the influence

of rotation on the density-driven plume. From the coastal surface plume literature, depending on the ratio of L_i to L_R, the plume can form a recirculating (cyclonic in the northern hemisphere) region near the river mouth and/or can propagate along the boundary in approximate geostrophic balance (Horner-Devine et al., 2006; Pimenta et al., 2011). In a lacustrine system, the width of the lake B can also impact the plume trajectory and modify the amount of mass trapped in a recirculating region relative to the transport in a boundary current. Dye studies of an inflow intrusion into a rotational, laboratory-scale model of Lake Iseo show that the intrusion plume is driven toward the lake boundary and the impact of rotation was characterized by a basin Rossby number based on the lake geometry ($Ro=u_{int}(fB)^{-1}$), rather than the river geometry, b, typically used for coastal plumes (Pilotti et al., 2014). A recirculating region was observed for small basin Rossby numbers in which the radius of deformation of the plume was approximately (or less than) the distance from the river mouth to the lake boundary (Pilotti et al., 2014).

Beyond the recirculating region, the intrusion can become a laterally-bounded geostrophic boundary current in which the cross-shore baroclinic pressure gradient is in balance with rotation. This region, which we will define as the far-field region, can transport material along the boundary in a geostrophic intrusion with a width given by $W \sim (QNf^{-2})^{1/3}$ (Imberger & Hamblin, 1982). The mid-field region is then defined as the region between the jet-like near-field plume and the far-field intrusion. In the far-field, the plume is laterally constrained by the geostrophic balance such that the intrusion thickness is more appropriately described by the 2D formulation (equation (2)). By substituting the geostrophic plume width (W) into equations (1) and (2), the geostrophic intrusion plume thickness and speed are given by

$$h_{int,g}=(QfN^{-2})^{1/3} \tag{5}$$

and

$$u_{int,g}=(QNf)^{1/3}. \tag{6}$$

In general, the mid- and far-field dynamics and transport from inflow intrusions in a wide system have been largely neglected in the literature, although this region can have a significant impact on the fate of sediments and other river-borne constituents. It is worth noting that there are different definitions of near-, mid-, and far-field in literature. We have chosen to use definitions based on the influence of rotation on the plume, as described above. Alternate definitions arise in the density current literature wherein the near-field is defined as momentum-dominated (i.e., before transitioning to a density current) and the far-field is defined as the density-driven (or intrusive) plume. In the present manuscript we have chosen to employ the definition based on the influence of rotation because we focus on intrusion transport dynamics rather than the initial mixing and dilution.

Sedimentation from a river plume largely follows the trajectory of the plume and the extent of sediment deposition, defined as the distance from the mouth at which sediment settles out of the water column, will depend on the dynamics of the plume. When the plume is rotationally constrained (as in the case of a recirculating plume), the extent of sediment deposition is constrained by the Rossby radius of deformation (Wells, 2009). When the plume is able to propagate away from the river mouth (without the influence of rotation or as a boundary current), the sedimentation extent is governed by plume characteristics and the sediment settling speed. For a plume that is not rotationally constrained, the extent of deposition L_{sed} can be approximated with

$$L_{sed} \approx u_p z w_s^{-1}, \tag{7}$$

where u_p is the plume velocity, z is some depth over which the sediment settles, and w_s is the sediment settling velocity (Geyer et al., 2004; Hill et al., 2000). According to Geyer et al. (2004), a distinction is made between surface and bottom trapped plumes because a surface trapped plume is not influenced by the bottom boundary layer, where bottom-generated turbulence helps to retain sediment in suspension (Geyer et al., 2004). Therefore, the relevant vertical scale z for a surface plume is proposed to be the surface plume thickness, h_p (Geyer et al., 2004). The assumption in this formulation is that, once sediment settles out of the plume (a distance h_p), it is no longer influenced by horizontal currents associated with the plume and is allowed to settle straight to the bed. In this manuscript, we will attempt to extend the formulation for the sedimentation extent (equation (7)) to the case of inflow intrusions using the intrusion speeds and thickness.

In the present manuscript, field observations and numerical modeling were used to study sediment transport from inflow intrusions into a stratified rotationally-influenced lake (Pallanza Bay of Lake Maggiore, Italy). The field observations provide time series measurements of currents, temperature, and suspended sediment concentration (SSC) along the intrusion plume over five inflow events. These events were used to validate a three-dimensional hydrodynamic and sediment transport model. Due to the importance of sedimentation extent on determining the impact of introduced constituents on an ecosystem, the main focus of the manuscript is to develop and evaluate a simple analytical expression to predict sedimentation extent from intrusions using only a priori known parameters in a real system. The analytical expression for sedimentation extent was compared to simulated sedimentation extent across a range of realistic scenarios using a validated numerical model. Additionally, the results from the numerical model are used to describe mid- and far-field plume dynamics and the impact of secondary dynamics on the transport and distribution of sediment within the bay.

2. Methods

2.1. Site Description

Extensive field observations were collected in Pallanza Bay, a large embayment in Lake Maggiore, Italy (see Figure 1). The study site is a rotationally-influenced lake with persistent ambient stratification and large sediment-laden river inflows. Lake Maggiore has a maximum depth of 375 m, and much of Pallanza Bay is approximately 120 m deep. The hydrodynamics in the lake are forced by winds, river inflows, seasonal heating and cooling, and rotation. The lake remains stratified year round and has only overturned three times in the past 50 years (Ambrosetti & Barbanti, 1999), although the stratification varies seasonally. The

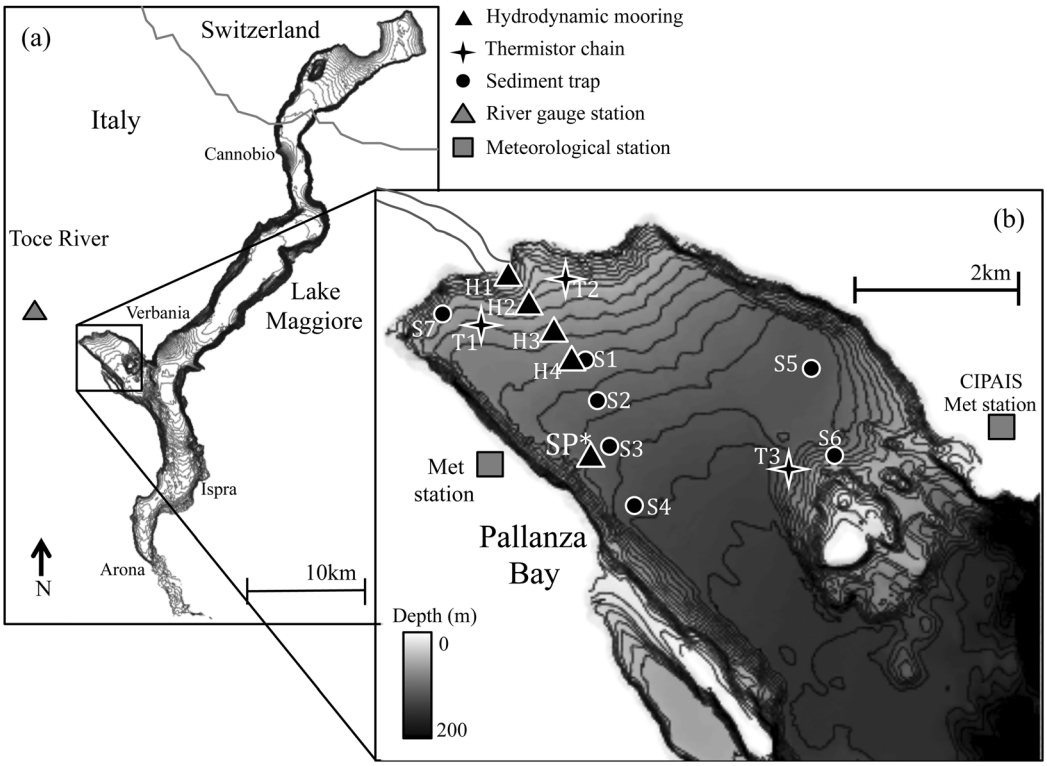

Figure 1. Bathymetry of Lake Maggiore (a) and Pallanza Bay (b) showing contours every 10 m. The extents of panel (b) are 45.89° to 45.94° N latitude and 8.48° to 8.56° E longitude. The Toce River gauge station is indicated by the gray triangle in (a). Black triangles in (b) indicate locations of hydrodynamic moorings (H1–4) from 2014, and SP* indicates the location of the South Pallanza mooring from 2012. These moorings measured currents, temperature, and SSC. Also indicated in (b) are thermistor chain mooring locations T1–3 (black stars), sediment trap locations S1–7 (black circles), and meteorological stations (gray squares), all deployed in 2014.

thermocline depth is typically between 20 and 50 m and the temperature difference between the top and bottom of the lake typically ranges from 5 to 20°C (Ambrosetti & Barbanti, 1999; Bertoni, 2009).

Pallanza Bay is relatively sheltered from large-scale motions in Lake Maggiore and large-scale internal wave activity is negligible (Scheu et al., 2015). Typically the Wedderburn number is large ($W > 10$), in which case the wind is expected to stir the surface waters without generating coherent thermocline tilting required to induce internal waves (Imberger & Hamblin, 1982; Imberger & Patterson, 1990). Additionally, the period of the first-mode internal wave in Lake Maggiore is 2–4 days (based on temperature observations). Therefore, long duration winds would be required to generate significant tilting and coherent internal wave activity (Imberger & Patterson, 1990). Wind and meteorological data were obtained from a permanent meteorological station on the northeastern side of the bay operated by CIPAIS (Commissione Internazionale per la Protezione delle Acque Italo-Svizzere) (Bertoni, 2009). A second meteorological station measuring wind speed and direction was deployed on the southwestern boundary of the bay from July to November 2014 (see Figure 1 for locations). The primary observed wind direction was southeasterly along the main axis of the bay at approximately 30° south of East. These winds are the primary driver of thermocline motion in the bay and frequently generate upwelling followed by relaxation (or downwelling in the case of wind reversal) (Scheu et al., 2015). Although the thermocline motions can generate small amounts of local resuspension in the bay at or near the depth of the thermocline, river inflow events are the primary drivers of sediment transport, a handful of which dominate the annual sedimentation in the bay (Scheu et al., 2015).

The Toce River is the primary inflow into the lake and is influenced by hydropower dams and reservoirs approximately 100 km upstream of the mouth, which is approximately 10 m deep and 200 m wide. The other large inflow into Lake Maggiore is the Ticino River, which enters at the northern end of the lake. The primary outflow is at the southern end of the lake, where water drains into the Ticino River. Large inflow events from the Toce River typically occur during the spring snowmelt season in May and June and during fall storm events in October and November (Bertoni, 2009, 2007). The sediments entering Pallanza Bay from the Toce River are largely composed of silts and clays. Erosion in the lake by river currents is small relative to the incoming sediment loads, with limited erosion occurring only near the Toce River mouth (Jones, 2012).

2.2. Field Observations

Moored instrumentation was deployed in Pallanza Bay during the fall of 2012 and the spring and fall of 2014. Time series data of velocity, temperature, and SSC collected over a total of 9 months are primarily utilized here for the purposes of model validation. During the 2012 deployment, three moorings were deployed from 12 October 2012 to 15 December 2012 to measure currents, temperature, and SSC. Details of these moorings and the 2012 field deployment and instrumentation setup are documented in Scheu et al. (2015). In the present manuscript, we focus on data from the mooring near the southern shore of Pallanza Bay at a depth of 120 m (South Pallanza site; SP* in Figure 1b). Two additional field deployments were conducted from 11 April to 7 July 2014 and from 23 July to 18 November 2014 with a total of seven hydrodynamic moorings and seven sediment traps (Figure 1b).

During the observation periods (indicated by the gray regions in Figure 2), six inflow events were observed in excess of 300 $m^3\ s^{-1}$, a flow rate that is approximately a twice-yearly flood event based on flood frequency analysis. The peak annual flows observed in the Toce River are typically 700-1,000 $m^3\ s^{-1}$ and typically occur during the spring snowmelt. The exception was year 2014, which experienced a relatively mild spring event (Q_{max}= 485 $m^3\ s^{-1}$) compared to the three previous years (2011–2013). The weak spring flood was followed by an unusually heavy rainfall season in the fall of 2014. In fact, the peak flow observed during the four-year record (Figure 2) occurred on day 316 of 2014, which corresponds to a five-year flood event.

The 2014 field sampling included three hydrodynamic moorings that were deployed with an upward looking acoustic Doppler current profiler (ADCP), 1–2 downward looking acoustic Doppler velocimeters (ADVs), and a chain of SeaBird thermistors (sites H2, H3, and H4 in Figure 1b). An additional hydrodynamic mooring was deployed at the river mouth (site H1) and housed an acoustic Doppler profiler (ADP), a laser in-situ scattering transmissometer (LISST), an optical backscatter sensor, and a SeaBird thermistor. Three additional thermistor chains were deployed at sites T1, T2, and T3. We focus on data from moorings H1 (8 m depth) and H3 (40 m depth) because these were used for model validation. Ten thermistors that sampled every 2 s were distributed in the vertical at site H3 with 2 m resolution in the bottom 10 m and with 5 m resolution

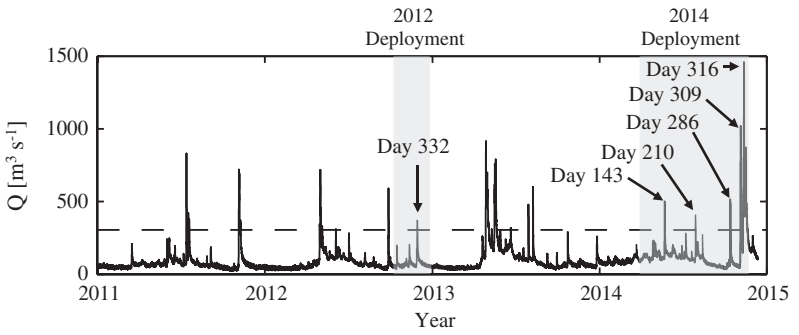

Figure 2. Toce River flow rate measured at the Candoglia gauge station (shown in Figure 1; flow rate data provided by Ramboll Environ, Italy), with the dashed line indicating the twice-yearly flood (300 $m^3 s^{-1}$). Gray shaded regions indicate the deployment periods in 2012 and 2014. Arrows indicate the date corresponding to the peak flow rate during the six observed events that are discussed in the text.

throughout the rest of the water column. The 600 kHZ Teledyne RDI ADCP at site H3 sampled at 10 s intervals with 6 pings per sample and with 2 m vertical resolution. Instrumentation at site H1 included a 2 MHz Nortek ADP (10 min sampling with 0.5 m vertical resolution) and a near-bed thermistor with a pressure sensor (1 min sampling) to measure inflow temperature. The shallow river is typically well mixed during inflow events based on temperature profile measurements in 2012.

The acoustic backscatter (ABS) intensity from the ADCP was used as a proxy for SSC once the raw backscatter intensity signal was processed for acoustic attenuation with distance from the transducer head (Gartner, 2004; Wall et al., 2006). Although an automated water sampler was deployed to directly measure SSC at site H3 to calibrate the measured ABS, it failed due to a manufacturing issue. The ADCP acoustic backscatter data were adjusted for beam spreading and acoustic absorption with depth following the procedure outlined in Gartner (2004) and Wall et al. (2006). The specific instrument and the deployment settings specify the beam spreading while the acoustic absorption coefficient varies as a function of temperature. Therefore, the temperature measured by the adjacent thermistor chains was interpolated to the ADCP bin depths and used to calculate attenuation coefficients as a function of depth and time during the deployment. There are a few gaps towards the end of the thermistor records due to faulty batteries and these gaps were linearly interpolated in the vertical.

Cylindrical sediment traps (15 cm in diameter and 1 m tall) were also deployed in duplicate at 3 and 10 m above the bed for the duration of the two sampling periods (black circles in Figure 1) (Lin et al., 2017). The mass and deposition thickness in the sediment traps were recorded at the end of the two deployment periods (Lin et al., 2017). We note that there is inherent uncertainty in comparing deposition rates because sediment traps, particularly the cylindrical ones used, can significantly overestimate net deposition (Flower, 1991; Kozerski, 1994). This is particularly true for larger particles and in locations with significant bottom stresses, such as in shallow areas of the bay. Therefore, the shallow traps near the mouth (S1 and S2), which can experience larger bottom stresses due to the river plume, are more likely to overestimate sediment deposition, particularly for coarser sediment grains (Flower, 1991; Kozerski, 1994;).

2.3. Model Description

The three-dimensional, unstructured-grid, finite-volume SUNTANS model (Fringer et al., 2006) was employed with the addition of a sediment transport module to study the deposition dynamics in Pallanza Bay. The SUNTANS model was utilized in hydrostatic mode and solves the Navier-Stokes equation with the Boussinesq approximation along with a free surface and employs an unstructured grid in the horizontal and a z-level or Cartesian grid in the vertical. As shown in Figure 3a, the model domain did not include the entire lake because of the relatively small influence of large-scale dynamics on the bay. However, the domain was extended to include the eastern boundary of the lake to prevent boundary effects associated with wind-driven upwelling of the thermocline. Model open boundaries in the lake were constrained with a fixed water depth to allow flow in and out of the domain and are indicated by the gray lines in Figure 3a.

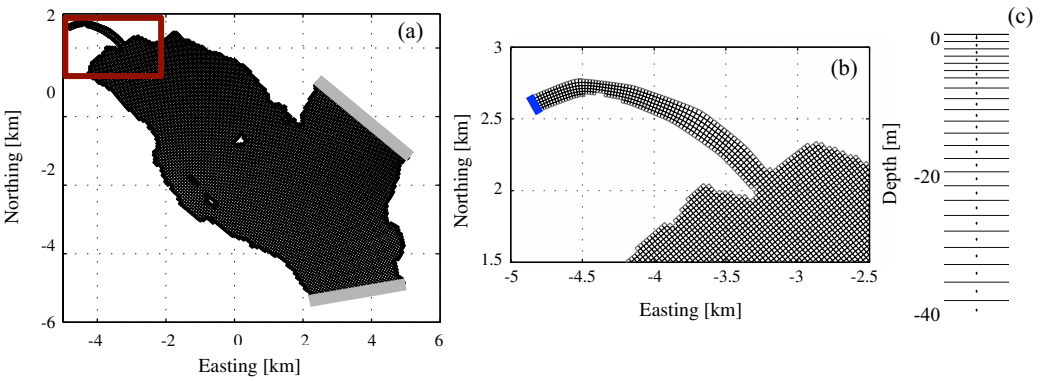

Figure 3. Model domain used for the numerical simulations (a) and a zoomed-in view of the river mouth (b). Gray lines in (a) indicate open boundaries and the blue line in (b) indicates the inflow boundary. The upper 40 m of the vertical grid with stretching is shown in (c).

The unstructured quadrilateral grid in Figure 3 was generated with GridGen (Lien et al., 2015) and had an average grid spacing of 40 m in the horizontal. A finer grid resolution with 20 m average grid spacing in the horizontal was also employed. However, the coarser grid was sufficient to resolve the dominant features of the plume in the model validation combined with the fact that the model validation metrics did not change appreciably with finer resolution, the coarser grid was used for the results presented. The vertical grid consisted of 60 vertical z-levels where the top 5 m of the water column had 1 m vertical resolution to resolve the shallow river inflow. 30 vertical z-levels were gradually stretched from 5 to 60 m depth (the deepest extent of the observed intrusions) and then more rapidly stretched from 60 m to the deepest portion of the domain with a depth of 350 m. A total of 461,365 grid cells were employed over the whole domain in 3D with 11,105 in the horizontal.

The horizontal eddy-viscosity was set to a constant ($\nu_h = 10^{-2}$ m^2 s^{-1}) and the vertical eddy-viscosity was computed with the Mellor and Yamada level 2.5 (MY 2.5) turbulence closure scheme (Mellor and Yamada, 1982). A background vertical eddy-viscosity was specified as $\nu_v = 10^{-6}$ m^2 s^{-1}. The Canuto-A stability function (Canuto et al., 2001) was used with the MY2.5 turbulence closure scheme to parameterize the effects of stratification on vertical mixing. This stability function has been shown to perform better in stratified environments compared with other stability functions such as that of Kantha and Clayson (Wang et al., 2011). Indeed, we found that the Canuto-A stability function more accurately reproduced the along-axis velocity and plume intrusion thickness than the Kantha and Clayson stability function. Advection of momentum and scalars was computed with a flux-limiting scheme following the method described in Chua and Fringer (2011).

To capture the period of the inflow events that lasted for roughly 2 days, simulations were run for a total of $t_{max} = 10$ days to allow full development of the plume dynamics and sufficient time for a large fraction of the incoming sediment to have settled. The simulation time step was dictated by the Courant number related to stability of explicit momentum advection, and was set to 10 s for inflow events less than 800 m^3 s^{-1} and 5 s for stronger events. Finally, a constant Coriolis parameter $f = 1.05 \times 10^{-4}$ rad s^{-1} was used for all simulations, corresponding to a latitude of 46°N.

2.3.1. Sediment Transport

Although bed load may be important in the river and near the river mouth where bed stresses and coarser particles are present, observations from Jones (2012) indicate that the sediments found throughout Pallanza Bay are composed of predominantly silts with some fractions of fine sands and clays. Therefore, we neglect bed-load transport and restrict our simulations to suspended sediment transport using three sediment size classes. The model particle size distribution was informed using a Beckman Coulter LS Particle Size Analyzer (after the organic content had been removed by conducting a peroxide burn-off) to measure sediment size distributions of samples from the sediment traps deployed in Pallanza Bay. The sediment size distributions from multiple sediment traps was averaged to specify the sediment size classes in the model. The median particle size (d_{50}), the Stokes settling velocity for each size class ($w_{s,m}$) (Stokes, 1851), and the percentage of each size class in the incoming sediment load are shown in Table 1. Because the settling velocity

Table 1
Incoming Sediment Load Characteristics Based on Measurements From the Toce River (Jones, 2012; Lin, 2015) *With Three Grain Size Classes and Where w_s Is the Stokes Settling Velocity*

	% Load	d_{50} [μm]	w_s [m s^{-1}]
Fine Sand	32	150	2.2×10^{-2}
Coarse silt	56	60	2.2×10^{-3}
Fine silt	12	16	1.4×10^{-4}

determines the distance into the bay that sediment is transported before it settles, the particle size affects the distribution of sedimentation in the bay. Although the settling speed may be impacted by flocculation and convective sedimentation effects (Fox et al., 2004; Guo & He, 2011; Scheu et al., 2015; Davarpanah and Wells, 2016), constant settling velocities are used for each sediment size class.

The transport of suspended sediment associated with size class $m=1,\ldots,N_s$, where $N_s=3$ size classes, is computed by solving the suspended sediment transport equation

$$\frac{\partial C_m}{\partial t}+\nabla\cdot(\mathbf{u}C_m)-w_{s,m}\frac{\partial C_m}{\partial z}=\frac{\partial}{\partial z}\left(K_C\frac{\partial C_m}{\partial z}\right), \tag{8}$$

where $\mathbf{u}$ is the three-dimensional Cartesian velocity vector, C_m is the SSC of size class m (in mg L^{-1}), $w_{s,m}$ is the settling velocity of size class m (where $w_{s,m}>0$), and K_C is the vertical eddy-diffusivity of sediment, which we assume is equal to the vertical eddy-diffusivity computed by the turbulence model.

Due to the importance of sediment on the density of the river relative to that of the lake on the inflow dynamics, the effect of the SSC on the density was included in the equation of state, such that the fluid density in the SUNTANS model was given by

$$\rho=\rho_T+\left(1-\frac{\rho_0}{\rho_{sed}}\right)\sum_{m=1}^{N_s}C_m, \tag{9}$$

where $\rho_0=1000$ kg m^{-3} is the reference density and $\rho_{sed}=2000$ kg m^{-3} is the dry density of the sediment mixture in the bed in Pallanza Bay (Lin et al., 2017). In the absence of suspended sediment, ρ is given by ρ_T, which is calculated by the UNESCO nonlinear equation of state as a function of temperature (Millero & Poisson, 1981; Millero et al., 1980). In Pallanza Bay and similar systems, the densimetric effect of sediment can account for as much as half of the total density variability of the incoming river plume.

Sediment deposition on the bed for size class m is computed at each time step with $D_m=w_{s,m}C_{bed,m}$, where the SSC at the bed for size class m, $C_{bed,m}$, is defined at the bottom face of the bottom cell. Because the SSC is stored at the cell centers, $C_{bed,m}$ is extrapolated from the two interior cells with $C_{bed,m}=1/2(3C_{m,N_k}-C_{m,Nk^{-1}})$, where N_k is the index of the bottom-most grid cell. The critical bed shear stress for sediment erosion from the bed was assumed to be constant throughout Pallanza Bay for each size class and given by $\tau_c=0.1$ Pa based on SedFlume measurements of critical shear stress from sediment cores taken throughout Pallanza Bay (Jones, 2012). The bed shear stress (τ_{bed}) in the model is computed using a quadratic drag law along with the law of the wall the law of the wall with a bottom roughness $z_{0,B}=0.005$. Sediment resuspension in Pallanza Bay is generally limited to the region near the Toce River mouth. Resuspension was also observed in small portions of the bay that experience erosional stresses due to wind-driven upwelling, although these events have a negligible contribution to the overall sedimentation dynamics (Scheu et al., 2015).

2.3.2. Boundary Conditions

The flow rate was specified at the Toce River mouth using data shown in Figure 2. The inflow temperature for the 2014 events was specified as the average temperature measured at site H1 over the validation event and is indicated by the dashed line in Figure 4. In general, the inflow temperature ranges from 9–14°C and is slightly colder in the winter and early spring (Figures 4a and 4b) and becomes warmer in the summer and early fall (Figures 4c–4e). The inflow sediment load was measured with two turbidity sensors installed in March 2014 by the Instituto Politecnico di Milano at the Gravellona Toce bridge (approximately 100 m from the mouth) (Jones, 2012). The SSC measured at this station was used to specify the incoming sediment loads for the events modeled in 2014, which gave the sediment rating curve $C=0.56Q$, with Q in m^3 s^{-1} and C in mg L^{-1} (Jones, 2012).

The initial vertical temperature structure was spatially uniform and obtained with a least-squares fit to the observed data, averaged over one day prior to each event, assuming the function $T(z)=T_0+\Delta T\tan^{-1}\left(\frac{z-z_0}{\delta}\right)$. As shown in Figure 4, this function accurately reflects the stratification in the lake throughout the 2014 observational period. The bottom temperature at 120 m depth was fixed at 6°C based on measurements of deep

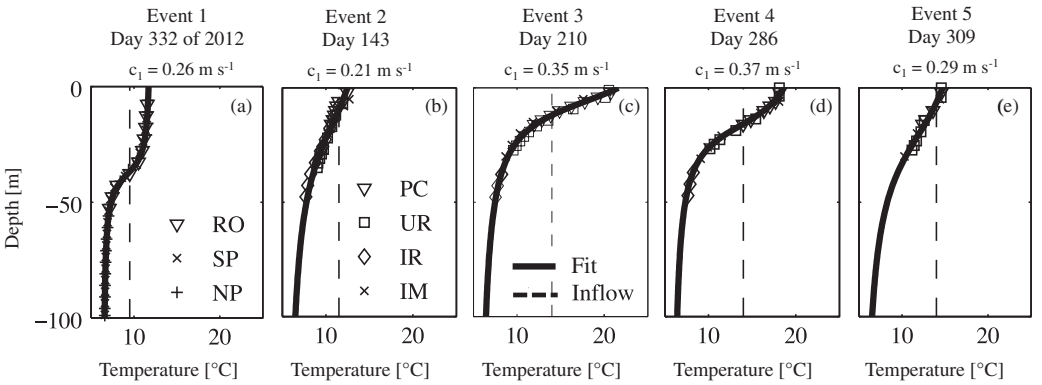

Figure 4. Ambient temperature structure for the observed events as a function of depth. The markers indicate field observations averaged over the day prior to the event at the indicated mooring locations. A least-squares fit to the data was used as the stratification for each event in the model (solid line) and the temperature measured at site H1 averaged over the event was used as the model inflow temperature (dashed line). The first-mode internal wave speed, c_1, was calculated assuming a depth of 120 m.

water in 2012. The lake is more stratified in the late spring through early fall (Figures 4c and 4d) as the surface warms and then becomes less stratified in the late fall and winter due to cooling and vertical mixing (Figures 4a, 4b and 4e). The strength of the stratification is characterized using the first-mode internal wave speed, c_1 (indicated in Figure 4), which was computed with a normal modes analysis (e.g., Fringer & Street, 2003) assuming 120 m water depth. Due to sparse temperature measurements during the day 316 flood event, the initial stratification for the day 316 simulation was assumed to be the same as for the day 309 event (Figure 4e).

The surface wind stress is specified using wind speed measured at approximately 10 m above the surface, assumed constant in space and computed with a quadratic drag law with a drag coefficient of C_d=0.0012 based on that of Large and Pond (1981). Wind speeds over water are expected to be larger than those measured at the two met stations on the banks of the bay (shown in Figure 1) because of sheltering by urban terrain in a mountainous environment (Shimizu et al., 2007). Therefore, the modeled wind forcing is the observed wind speed multiplied by a factor of 2.5 (Shimizu et al., 2007). Additionally, the average wind direction measured at the two stations indicates that the winds are largely channelized along the main axis of the bay such that the winds were directed either towards the southeast (30 degrees from East) or in the opposite direction towards the northwest. Therefore, the modeled wind speeds are magnified and oriented along the main axis of Pallanza Bay, consistent with Scheu et al. (2015).

2.4. Validation Performance Metrics

The numerical model was validated using a number of common performance metrics. The primary metric was the model skill score (Murphy & Epstein, 1989) (also termed model efficiency; Nash & Sutcliffe, 1970), which has been widely used to validate hydrodynamic models. The simulated temperature and velocity field were validated with the skill score, defined as

$$SS = 1 - \frac{\sum (x_{obs} - x_{sim})^2}{\sum (x_{obs} - \overline{x_{obs}})^2}, \tag{10}$$

where x_{obs} are observation data points, x_{sim} are the corresponding simulated data points, and $\overline{x_{obs}}$ is the mean value across all data points. The summations and the mean were computed across both depth and time over a 5-day validation period surrounding the event. According to Marechal (2004), model performance can be characterized by the skill score as excellent (0.65-1), very good (0.5-0.65), good (0.2-0.5), poor (0-0.2), and very poor (<0), where negative values indicate that the model error variance exceeds the variance in the observations (Allen et al., 2007; Marechal, 2004).

The error metrics I_1 and I_2 (Rueda & Schladow, 2003) have also been commonly used to validate the temperature structure of numerical models in lacustrine systems (Laborde et al., 2010; Morillo et al., 2008; Rueda & Schladow, 2003). In fact, much of the numerical modeling of inflows into lakes has relied on validation of the temperature structure alone. Acceptable values of I_1 and I_2 for model validation range from 0.03-0.06 in

the literature (Laborde et al., 2010; Morillo et al., 2008). The RMS error (RMSE) and bias were also computed for the velocity signal as utilized in Rayson et al. (2015). All of the velocity performance metrics were computed using the along-axis velocity (the coordinates were rotated using principle component analysis to the principle axis) for both the observations and simulations.

Recall that SSC was not directly measured, but instead the measured ABS from the ADCPs was used as a proxy for SSC. Therefore, the modeled SSC was validated with the measured ABS using the correlation coefficient (CC) defined by

$$CC = \frac{1}{N}\frac{\sum(x_{obs} - \overline{x_{obs}})(x_{sim} - \overline{x_{sim}})}{\sigma_{sim}\sigma_{obs}}, \tag{11}$$

where σ_{obs} and σ_{sim} are the standard deviations of x_{obs} and x_{sim}, respectively. For reference, CC corresponding to $p = 0.1$ ($df = 15$) is approximately 0.41 (there is slight variability in the auto-correlation for each event and therefore the largest CC value is shown here to be conservative). Although not a direct validation, the correlation coefficient indicates model ability to capture trends in the sediment dynamics. Results of the model validation are discussed below.

3. Model Validation and Scenarios

The numerical model was validated using the five observed inflow events captured during nine months of data collection in Pallanza Bay. During the observation periods (indicated by the gray regions in Figure 2), six inflow events were observed in excess of 300 $m^3\ s^{-1}$, a flow rate that is approximately a twice-yearly flood event based on flood frequency analysis. The twice-yearly flood was chosen as the threshold for event analysis and model validation (dashed line in Figure 2) because these events are large enough to significantly contribute to the annual sedimentation in the bay (Scheu et al., 2015) while still providing an adequate number of events for model validation. Unfortunately, the data from the five-year flood event (on day 316 of 2014) is relatively incomplete due to massive amounts of sediment accumulation and debris on the instrumentation during the event, which also led to significant flooding of nearby structures because the lake level rose by 6 m. The day 316 event also occurred during recovery when some instrumentation was out of the water, and a number of the instruments had depleted their batteries by this time. Therefore, while all six events were simulated and the corresponding sedimentation dynamics will be discussed, only five of the six observed events were quantitatively validated with the numerical model. The stratification and inflow conditions for all observed events are shown in Table 2 including the densimetric Froude number (which includes the densimetric effect of sediment loading) and the basin Rossby number.

Performance metrics were computed to assess the ability of the model to capture the dynamics and sediment transport of observed inflow intrusions. To compute the metrics for velocity and SSC, the observations at site H3 were averaged over 10 min intervals to reduce instrument noise while still resolving the inflow variability. Temperature measurements were averaged over one-minute intervals. Model results (x_{sim}) were subsampled in time (to match the observed data frequency) and interpolated to the depth of the observations before computing the performance metrics, which are shown for all of the validation events in Table 3.

Table 2
Observed Events With Relevant Parameters Including the Maximum Flow rate, Q_{max}, the Ambient Stratification Characterized by the First-Mode Internal Wave Speed, c_1, Inflow Temperature, T_{in}, the Inflow Densimetric Froude Number, Fr, and the Intrusion Basin Rossby Number Based on the Bay Width, Ro

Event	Type	Day of Year	Q_{max} [$m^3\ s^{-1}$]	c_1 [$m\ s^{-1}$]	T_{in} [$^\circ C$]	*Fr*	*Ro*
1	Far-field	332 (2012)	360	0.26	9	0.76	0.81
2		143 (2014)	485	0.21	11.5	1.28	1.01
3	Near-field	210 (2014)	375	0.35	14	0.53	0.88
4		286 (2014)	440	0.37	14	0.68	0.98
5	Extreme	309 (2014)	985	0.29	11	2.44	2.51
6	Incomplete	316 (2014)	1350	0.29	11	3.52	3.66

Table 3
Performance Metrics for the Five Validation Periods

	2012 Data		2014 Data		
Day of year	332	143	210	286	309
Event#	1	2	3	4	5
Temperature					
SS	0.89	0.57	0.95	0.77	0.71
I_1	0.05	0.06	0.04	0.01	0.05
I_2	0.08	0.06	0.06	0.12	0.07
n	25920	61200	29160	29160	22981
Axial velocity					
SS	0.52	0.46	0.55	0.59	0.65
RMSE [m s^{-1}]	0.07	0.05	0.05	0.06	0.18
Bias [m s^{-1}]	0.03	0.04	0.01	0.01	0.05
n	9072	6480	8424	8424	5030
SSC					
CC	0.78	0.82	0.71	0.60	0.88
n	9072	7056	8424	8424	5030

Note. *n* indicates the number of data points for each variable.

For brevity, we focus on discussion of two of the five events with an emphasis on model limitations in what follows. Model behavior for the other three events is similar.

3.1. Validation Events

Of the five validation periods, the skill scores for velocity and temperature for Event 2 (Figure 5) were the lowest because of the difficulty in correctly capturing the depth and timing of the intrusion. During this event, the inflow intruded relatively deep in the water column due to a large sediment load (500 g m^{-3}) despite a warm inflow temperature (T_{in}=11.5°C) relative to the ambient. The plume plunges downward during the peak in flow and sediment concentration and then abruptly returns to a depth of neutral buoyancy after the large sediment load propagates past the mooring. There was also an along-axis wind that began on day 141 and drove thermocline upwelling, which can be seen by the cool temperatures moving upward through the water column on day 142. The dynamics of this event are particularly difficult to model because the depth of the plume is sensitive to small changes in SSC (owing to sediment-induced density effects)

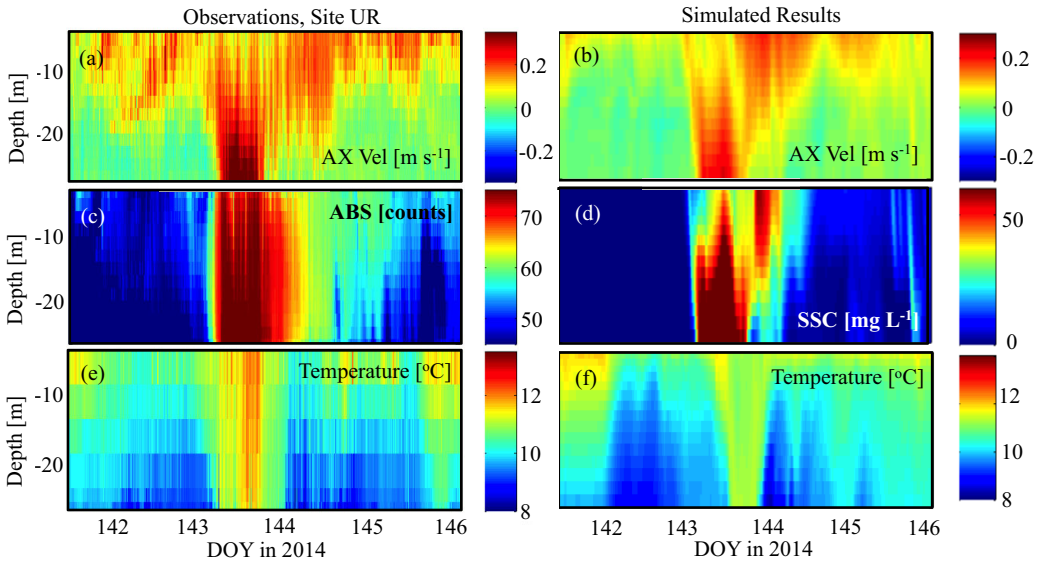

Figure 5. Comparison of observed (left) to modeled (right) data during validation Event 2.

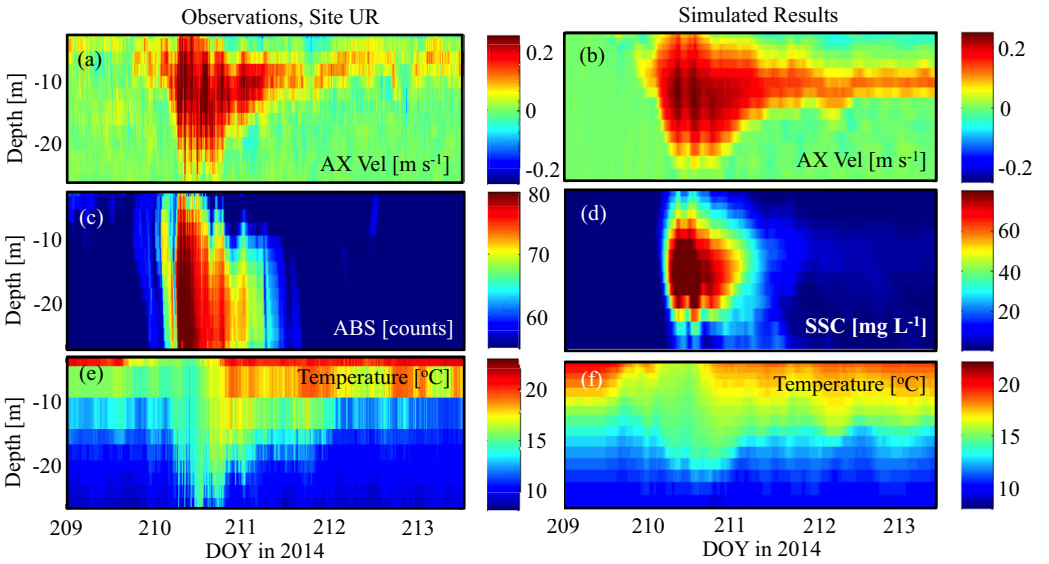

Figure 6. Comparison of observed (left) to modeled (right) data during validation Event 3.

and the timing of upwelling. Observations of the plume indicate high-frequency variability in velocity and temperature measurements. The timing of these high-frequency fluctuations is challenging to accurately capture in the numerical model and can lead to a lower skill score, even when the magnitude of the fluctuations is correctly reproduced. Furthermore, large velocities are present in the observations before the inflow event begins. Nevertheless, the simulations correctly capture the overall movement of the plume through the water column as the SSC and density of the plume change, as indicated by the skill score values in the good to very good range. The correlation coefficient for SSC is high, indicating that the model accurately resolves sediment transport in the plume.

Good skill scores do not always reflect good agreements during all points in time, as demonstrated during validation Event 3 (Figure 6). During this event, the inflow was less dense (warmer with a smaller sediment load) and the ambient water column was significantly more stratified. Wind forcing generated upwelling and subsequent relaxation of the thermocline during the peak in the flow rate, which alters the intrusion thickness. The validation metrics for Event 3 were good for temperature, velocity, and SSC and the model reproduced the changes in intrusion thickness over the course of the event as well as the intrusion depth. The SSC correlation coefficient is high, indicating that the model correctly reproduces the sediment transport dynamics. Qualitatively, however, the modeled sediment plume does not extend down to the sediment bed as it does in the observations (Figure 6). This discrepancy may be due to flocculation or convective sedimentation, which are not resolved in the numerical model but can act to enhance the particle settling velocity (Scheu et al., 2015). The discrepancy could also be due to uncertainty in using ABS as a proxy for SSC because ABS is sensitive to both variation in particle size and other constituents in the water column. The numerical model may slightly over predict the sedimentation extent from inflow plumes due to under prediction of the effective settling speed. To better validate the sedimentation dynamics, we compare simulated deposition to that observed in the sediment traps, discussed below.

Despite the limitations highlighted above, for all events the skill of the model at reproducing the temperature structure fell between very good and excellent (0.57-0.95), while the modeled velocity ranged from good to very good (0.47-0.65). We note that, as far as we are aware, this is one of the most extensive validations of currents, temperature, and SSC in a real field-scale intrusive sediment-laden plume to date in the literature. In general, the good to excellent model skill scores across all validation periods indicate that the model accurately captures the velocity structure and intrusion depth, which indicates that the model is accurately capturing the near-field mixing and entrainment. However, the model compared less favorably with observations when changes in the plume density cause the plume to move vertically through the water column (Event 2; Figure 5). Vertical movement of the plume was more likely to occur when the lake

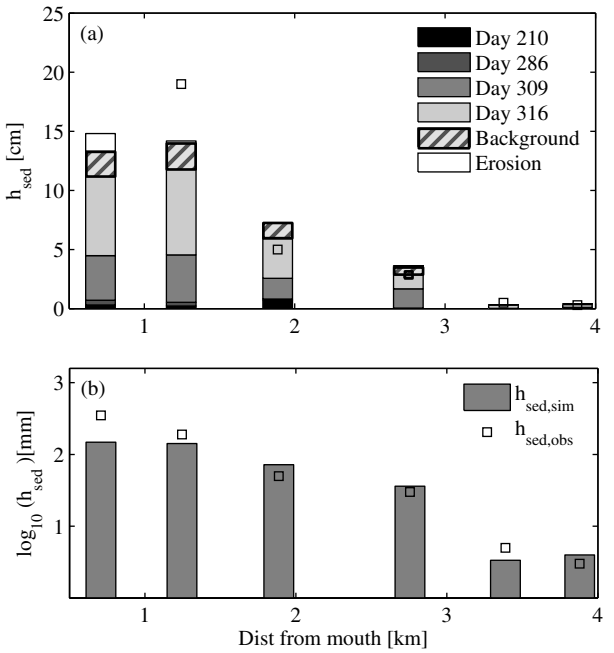

Figure 7. Measured (squares) and simulated (bar graphs) deposition during the fall period from 23 July to 18 November as a function of distance from the river mouth. The bar graph in (a) shows the contribution to the total simulated deposition of each simulated event during the fall deployment period, the background deposition, and simulated erosion. The total simulated deposition is also compared to measured sediment trap deposition on a logarithmic scale (b).

was less stratified and the intrusion depth was more sensitive to slight variations in density. Conversely, the vertical movement was more constrained and the model performed better when the lake was more stratified. Additionally, in some of the validation periods, we found that the simulated sediment plume did not extend to the sediment bed as was observed in portions of the data. As suggested above, this may be due to sediment processes not resolved in the model or uncertainties in the measured data.

3.2. Sediment Deposition From Observed Events

In addition to the performance metrics for plume dynamics, sediment transport for the modeled events was compared with the sedimentation observed at six sediment trap locations throughout the bay. While the validation events provide a good means of validating plume dynamics including intrusion speed, depth, and thickness, the proxy for sediment concentration, ABS, is not an adequate measure of model ability to compute SSC. Instead sediment transport was validated by comparing the simulated deposition thickness, $h_{sed,sim}$, to the measured deposition thickness from the sediment traps, $h_{sed,obs}$. The sediment traps were deployed in both the spring (8 April to 10 July) and fall (23 July to 18 November) deployment periods. The simulated and observed deposition are shown as a function of the sediment trap distance from the river mouth in Figure 7. Assuming that a few large inflow events contribute to the net sedimentation in Pallanza Bay, the measured deposition from the fall period was compared to the cumulative simulated deposition from the four events (Events 3, 4, 5, and 6 from Table 2) that occurred during the fall period (Figure 7a). The sediment deposition contribution from each discrete inflow event is shown in Figure 7a (shown on a linear scale to accentuate discrepancies between measured and simulated deposition). The large inflow events disproportionately contribute to the net sedimentation in the system, particularly at the shallower sites. This implies that the sedimentation is indeed dominated by the four discrete events.

In Figure 7a, we are comparing simulated deposition from four 10-day events (40 days) to measured deposition over a 120-day deployment period. To approximate the background deposition over the remaining 80 days, the simulated deposition over each event was scaled using the ratio of background base flow (100 m^3 s^{-1}) to the peak flow for each event. The average of the scaled sedimentation for all four events was used to estimate the background deposition over the 80 days not simulated (Figure 7a). As expected, the amount of background sedimentation and erosion are more significant at the shallower sites closer to the river mouth. These modifications improve the comparison between the simulated and observed sedimentation rates at the traps. However, there is still a discrepancy between the measured and simulated deposition at site S1, in particular (measured sedimentation at S1 is 35 cm and not shown in Figure 7a). This is likely because sediment traps overestimate sedimentation because they do not allow erosion once the sediment settles in column (Kozerski, 1994). Furthermore, excessive sedimentation in the model within the river prior to entering the bay may also account for some of the under prediction of sedimentation at the sediment trap location closest to the river mouth.

Simulated and observed sediment deposition are also shown on a logarithmic scale in Figure 7b to accentuate smaller deposition rates at the traps farther from the mouth. Although the simulated deposition under predicts the observed deposition at the shallower sites, the modeled deposition compares relatively well to the total observed sedimentation over the 120-day period and the trend across the traps is well captured, particularly when considering the large range of uncertainty and complexity in accurately capturing sedimentation rates in the mid- and far-field regions of the plume. The model also accurately captures deposition at sites S5 and S6 on the northern side of the bay, which requires accurately resolving secondary circulation patterns (discussed below). Therefore, while the model under predicts sedimentation near the river mouth, the model is accurately capturing the mid-and far-field sediment transport dynamics from the

inflow intrusion and provides confidence to investigate sedimentation over a wider range of inflow and stratification conditions, as discussed below. The model ability to reproduce intrusion dynamics and sedimentation in the mid- and far-field regions of the plume provides confidence to further investigate intrusion dynamics and sedimentation across a wider range of inflow and stratification conditions.

3.3. Model Scenarios

The validated numerical model was used to extend the results from the observed events to a wider range of scenarios with realistic inflow and stratification conditions. These scenarios are simplified versions of the observed events in order to remove the influence of wind and variable inflow conditions on the resulting sediment transport from inflow intrusions in Pallanza Bay. In this regard, a range of scenarios were explored using a self-similar hydrograph with varying initial and boundary conditions to better isolate the impact of inflow and ambient conditions on sediment transport. The model hydrograph in Figure 8 was developed by normalizing the event hydrographs by the peak flow rate, Q_{max}, and fitting the normalized flow rates with an exponentially modified Gaussian (Lan & Jorgenson, 2001; Marco & Bombi, 2001). The self-similar function characterizes long-tailed distributions and is given by

$$Q^*(t)=\frac{Q_0}{Q_{\max}}+\frac{V_0}{Q_{\max}}\exp\left(\frac{\sigma_g^2}{2\tau^2}-\frac{t-t_0}{\tau}\right)\times\operatorname{erfc}\left[\frac{1}{\sqrt{2}}\left(\frac{\sigma_g}{\tau}-\frac{t-t_0}{\sigma_g}\right)\right], \tag{12}$$

where V_0 is related to the magnitude of the peak flow, t_0 is the time of the peak flow rate (specified as $t_0=1$ day), σ_g is related to the width of the Gaussian curve, and τ is the decay rate of the exponential (Hanggi & Carr, 1985; Lan & Jorgenson, 2001). The parameter Q_0 is related to a base flow quantity to account for the non-zero flow before and after the events, which is approximately 50–100 $m^3\ s^{-1}$ in the dimensional time series.

The parameters for the model hydrograph given by equation (12) were fit using a nonlinear least squares method ($R^2=0.89$) to the normalized observed flow rates centered about the peak to give a maximum value of $Q^*(t)=1$. This idealized, non-dimensional curve captures realistic flow variability over the course of an event and can be scaled to simulate varying magnitude flow events by employing a simulated flow rate of $Q_{sim}(t)=Q_{\max}\times Q^*(t)$. Small, moderate, and large flow cases were simulated, corresponding to $Q_{\max}=$ 310, 620, and 930 $m^3\ s^{-1}$, respectively. These are within the range of observed flow rates and representative of approximately a twice yearly, 1-year, and 2-year flood event, respectively. The flow cases were chosen to induce significant sediment transport in the bay, although weak enough to ensure that the inertial length scale was smaller than the length of Pallanza Bay in order to observe the development of the far-field plume region. For the large flow case, the inertial length scale was roughly 10 km, on the order of the bay length.

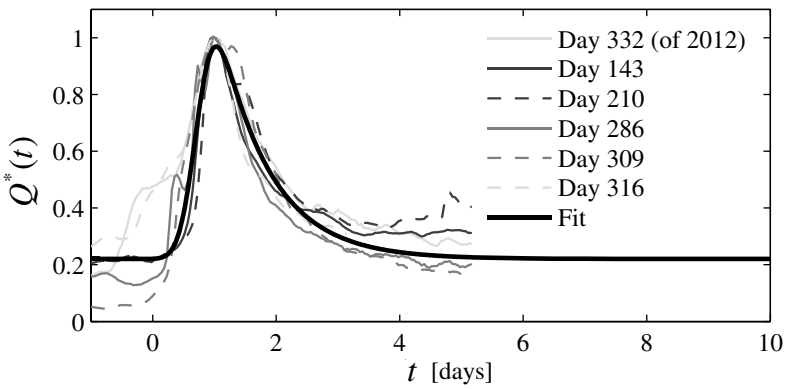

Figure 8. Observed flow rates from 2012 and 2014 normalized by their peak value (Q_{max}) and centered in time such that the maximum flow rate occurs on day 1 ($t_0=1$ day). The normalized hydrographs were fitted to the function shown in equation (1)2 with fit parameters of $V_0Q_{\max}^{-1}=2.63$, $Q_0Q_{\max}^{-1}=0.22$, $\sigma_g=0.23$ days, and $\tau=0.27$ days (solid black line with $R^2=0.89$).

Table 4
Model Scenarios Indicating the maximum Flow Rate, Q_{max}, Ambient Stratification Characterized By, c_1, the Inflow Temperature, T_{in}, the Densimetric Froude Number, Fr, and the Intrusion Basin Rossby Number, Ro

Run	Q_{max} [$m^3 s^{-1}$]	c_1 [$m s^{-1}$]	T_{in} [°C]	*Fr*	*Ro*
1	310	0.35	11 (cool)	0.61	0.69
2	310	0.35	14 (warm)	0.68	0.69
3	310	0.21	9 (cool)	1.54	0.67
4	310	0.21	11 (warm)	2.52	0.64
5	620	0.35	11 (cool)	1.20	1.40
6	620	0.35	14 (warm)	1.30	1.37
7	620	0.21	9 (cool)	0.89	1.38
8	620	0.21	11 (warm)	3.65	1.34
9	930	0.35	11 (cool)	1.82	2.19
11	930	0.35	14 (warm)	1.98	2.16
10	930	0.21	9 (cool)	3.76	2.15
12	930	0.21	11 (warm)	4.25	2.18

Two stratification conditions were used to study the effects of the temperature structure. The strong stratification case (early fall/late spring) was defined by the temperature structure observed on day 210 (Figure 4c) and the weak stratification case (early spring/late fall) was defined by the temperature structure observed on day 143 (Figure 4b). Additionally, two different river inflow temperatures were simulated (warm and cool) based on the range of inflow temperatures observed. During the weakly stratified spring events, the inflow temperatures tended to be colder (9–11°C) compared to warmer temperatures (11–14°C) observed during the strongly stratified fall events. The scenarios (shown in Table 4) are intended to represent the range of observed conditions in Pallanza Bay in order to realistically characterize the variability of the inflow and sedimentation dynamics. The sediment concentration was specified with the same sediment rating curve ($C = 0.56Q$; Jones, 2012) and the same sediment size class distribution (Table 1) as the validation events. It is also worth noting that the scenarios considered are limited to the case of intrusions and we have not considered underflow plumes or surface plumes because these have received more attention in the literature.

4. Results and Discussion

4.1. Intrusion Dynamics

For all scenarios indicated in Table 4, the inflow intrusion quickly transitions from a momentum-driven river plume to a density-driven intrusion within 0.4 km from the river mouth, even for the largest flow rate cases (with largest densimetric Froude number). In all cases considered, the river plume propagates into the lake before turning toward the southern boundary of the lake and propagating as a boundary current. The evolution of the plume for a representative scenario (Run 7 in Table 4) is shown in Figure 9. The scenario has a moderate flow rate ($Q_{max} = 620$ m^3 s^{-1}) with weak stratification ($c_1 = 0.21$ m s^{-1}) and a cool inflow ($T_{in} = 9^{\circ}C$). The plume intrudes into the water column within 250 m of the river mouth at approximately 30 m depth. At approximately 0.9 inertial periods (given by $(2\pi)^{-1}ft$, where $t = 0.6$ days is the elapsed simulation time), the plume has intruded into the water column, but is not yet significantly influenced by rotation (Figure 9a). This is consistent across all observed results, although the timing of the plume intrusion varies depending on river inflow conditions. At approximately 1.5 inertial periods ($t = 1$ day, which corresponds to the peak flow rate), the inflow intrusion has been deflected toward the southern boundary due to rotation (Figure 9b). A small recirculating region has also developed in which the flow is driven back toward the river mouth after the plume impinges on the southern boundary.

Two days into the simulation (2.9 inertial periods), the plume shown in Figure 9c is propagating along the southern boundary. It should be noted that the plume is constrained by a relatively shallow (10–15 m depth) sand bar near the two islands (see depth in Figure 1b), which acts as an effective boundary for the intrusion, which is at a depth of 30 m. Based on the extent of the boundary current relative to the near-field

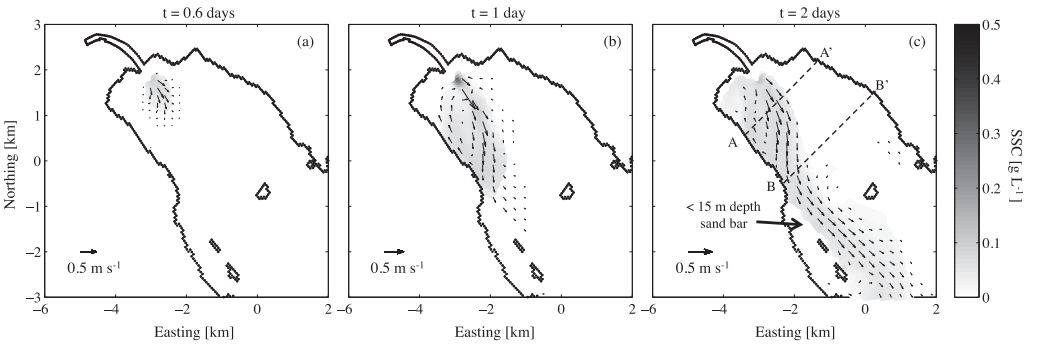

Figure 9. Temporal evolution of velocity vectors and SSC (grayscale) at the intrusion depth (30 m) for a representative scenario (Run 7) with a moderate flow rate (Q_{max} = 620 m^3 s^{-1}), spring ambient stratification (c_1=0.21 m s^{-1}), and a cool inflow (T_{in}=9°C). Snapshots are shown at t = 0.6 days (0.9 inertial periods) (a), t = 1 days (1.5 inertial periods) (b), and t = 2 days (2.9 inertial periods) (c). Plots along transects A-A′ and B-B′ are shown in Figure 10.

region, the plume dynamics and associated extent of sediment transport into Pallanza Bay appear to be largely dictated by the boundary current dynamics. Although boundary currents develop for all scenarios, the depth, thickness, and speed of the plume vary depending on the inflow and ambient conditions. For some cases, the intrusion depth is shallower than the island sand bar, which allows the plume to flow around the small islands in the southern region of the bay, leading to sedimentation there.

While rotation drives the plume toward and along the southern boundary, the intrusion speed and intrusion thickness are strongly influenced by the ambient stratification. To illustrate this, transects of velocity and SSC across the plume in the near- and far-field for both weak and strong stratification scenarios (Runs 5 and 7, respectively) are shown in Figure 10. Both scenarios have moderate inflows (Q_{max}=620 m^3 s^{-1}) and cool inflow temperatures, but have different initial stratification conditions. The velocity of the near-field intrusion (transect A-A′) is strongest approximately 1 km from the southern boundary for both scenarios. Although the plume for both cases has not been significantly influenced by rotation, the magnitude of the plume velocity varies between the strong and weak stratification conditions. The weakly stratified case (Figure 10b) results in a peak velocity of 0.21 m s^{-1}, while the strongly stratified case (Figure 10a) results in a peak velocity of 0.32 m s^{-1}. This is consistent with the scaling of the intrusion velocity for a laterally unconstrained plume (equation (4)), which implies that the intrusion speed and associated currents are expected to increase with increasing stratification. The intrusion velocity also increases as the volume inflow, Q, increases.

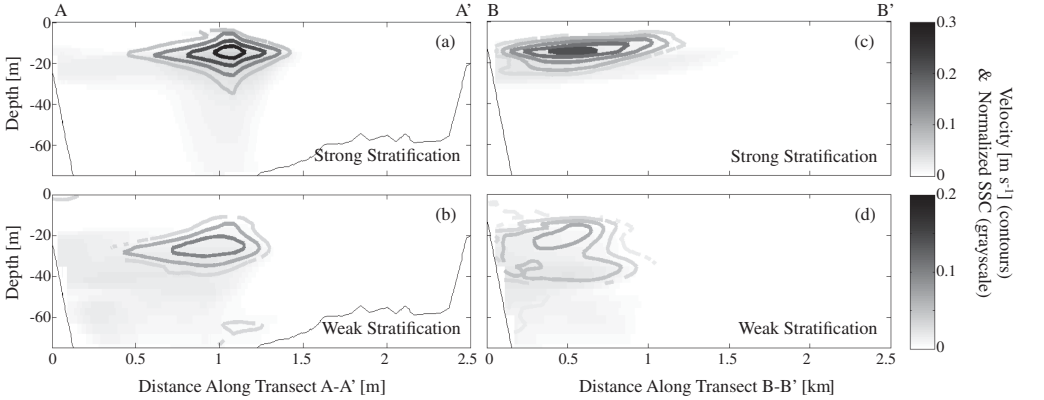

Figure 10. Lateral transects across the plume in the near-field (A-A′) on day 2 of the simulations of the velocity normal to the transect (contours) and normalized SSC (grayscale) for both strong (Run 5; a) and weak (Run 7; b) stratification scenarios (transect locations are indicated in Figure 9c). Far-field transects (B-B′) of velocity normal to the transect (contours) and normalized SSC (grayscale) are shown in (c) and (d) for the strong (Run 5) and weak (Run 7) stratification conditions, respectively.

In the near-field transect, the normalized SSC extends beyond the velocity contours. For example, in Figure 10a, there is a region of SSC to the left (toward the southern boundary) and below the velocity contours. The normalized SSC in this transect for the weaker stratification is also observed beyond the velocity contours, although the sediment is more evenly distributed in this case. The sediment below the velocity contours is due to sediment settling out of the plume, which increases over time. The sediment to the left of the velocity contours is due to the recirculation region that develops near the mouth and can be seen in Figuress 9b and 9 c. The velocities in this region are relatively small compared to those in the jet-like intrusion at approximately 1 km along the transect. While most of the sediment is transported beyond this recirculation region, a measurable quantity of sediment is transported back toward the mouth near the southern boundary in the recirculating region. The size of the recirculating region also varies with flow rate because weaker inflows have a smaller inertial length scale compared to stronger inflows, and hence weaker inflows are more strongly influenced by rotation.

The far-field transect in Figure 10 indicates the behavior of the plume where the intrusion is laterally bounded by rotation and the steep southern boundary of the bay (left side of transect B-B′). The intrusion velocity is again larger for the strongly stratified scenario (Figure 10c) compared to the weakly stratified scenario (Figure 10d) as indicated by the velocity contours. The intrusion thickness (vertical extent) is smaller for the strongly stratified scenario (Figure 10b) compared to the weakly stratified scenario (Figure 10d). Based on the velocity contours, the weakly stratified plume is approximately 30 m thick, while the strongly stratified plume is approximately 12 m thick, which is consistent with the inverse relationship between intrusion thickness and stratification. The warm inflow conditions for the moderate flow (Runs 6 and 8; not shown) behave similarly, although the intrusions occur slightly higher in the water column relative to Runs 5 and 7 (shown in Figures 9 and 10). In general, weaker stratification leads to a slower, thicker intrusion compared to stronger stratification. Based on these findings, the stratification is expected to play a significant role in the extent of sediment transport into the system.

4.2. Sedimentation Extent

Since the extent of sediment transport in Pallanza Bay is largely governed by inflow intrusions where the plume is either laterally unconstrained or propagating along the southern boundary, an analytical expression was developed to estimate the extent of sedimentation for the model scenarios. The analytical expression for sedimentation extent for a buoyant plume (equation (7)) proposed by Geyer et al. (2004) is extended to the case of transport from inflow intrusions by using the appropriate plume speed and vertical length scale. The plume thickness is used as the relevant vertical scale because the bay is deep relative to the intrusion depth or plume thickness (Geyer et al., 2004). By substituting the appropriate plume speed and thickness, the expected sedimentation extent is given by

$$L_{sed,lu} \sim \left(\frac{Q^2 c_1 \pi}{D}\right)^{1/3} \frac{1}{w_s} \tag{13}$$

for a laterally unconstrained intrusion (using equations (3) and (4)) and by

$$L_{sed,g} \sim \left(\frac{Q^2 f^2 D}{c_1 \pi}\right)^{1/3} \frac{1}{w_s} \tag{14}$$

for a geostrophic intrusion (using equations (5) and (6)).

In the above expressions, Q is defined as the inflow volumetric flow rate for simplicity, although this value could be modified to account for near-field entrainment and mixing. Additionally, the value of N defined as the buoyancy frequency across the intrusion (Ford & Johnson, 1983; Imberger & Hamblin, 1982), has been approximated with a more general representation of the ambient stratification embodied in the first-mode internal wave speed, c_1. Since N depends on knowledge of the intrusion depth and the plume thickness, we have employed c_1 to simplify the expression and minimize the need for a priori knowledge of the plume dynamics. As mentioned previously, the first-mode internal wave speed was computed for each of the stratification conditions (Figure 4) using the average water column depth ($D = 120$ m) in Pallanza Bay. Using this first-mode internal wave speed, the effective stratification is approximated with $N = c_1 \pi D^{-1}$ based on linear theory for constant N, implying $c_1 = ND\pi^{-1}$. This ensures that N is a more generalized measure of the ambient stratification in the system and does not require an assumption of the depth at which N is computed.

As a result, the intrusion dynamics can be evaluated without knowledge of the complex near-field mixing dynamics. While the near-field mixing dynamics can be partially taken into account by modifying the volumetric flow rate Q to include near-field dilution (which would also incorporate the effects of inflow temperature), the general stratification parameter works reasonably well across the wide range of inflow and stratification conditions observed in Pallanza Bay.

For completeness, the sedimentation extent can be naively approximated with the near-field river inflow parameters. The near-field sedimentation extent expression is a function of the river inflow speed ($u_0 = QA^{-1}$, where A is the cross-sectional area of the river mouth) and the river depth h_0 and is given by

$$L_{sed,0} \sim \frac{QA^{-1}h_0}{w_s}. \tag{15}$$

The simulated extent of sediment deposition, L_{sed}, from the model scenarios (Table 4), was approximated as the distance from the river mouth at which 50% of the sediment entering the bay (sediment deposition within the river was not included in the computation) had deposited. Comparison of the expected to simulated sedimentation extents is shown for the smallest sediment size class ($w_s = 1.4\times10^{-4}$ m s^{-1}) in Figure 11. The simple analytical expression using the scaling arguments for intrusion velocity and thickness in a laterally unconstrained system (equation (1)) captures the trend in sedimentation extent from the scenarios as indicated by the least squares fit to the data ($R^2 = 0.80$, where $R^2 > 0.5$ corresponding to $p = 0.01$) and shown in Figure 11a better than the geostrophic plume speed (equation (14); $R^2 = 0.25$) shown in Figure 11b. The sedimentation extent based on river inflow parameters (equation (15)) poorly predicted the sedimentation extent (Figure 11c; $R^2 = 0.15$) because it scales with Q as opposed to $Q^{2/3}$ and does not take into account the ambient stratification. The laterally unconstrained expression best predicts the sedimentation extent, indicating that the extent of the center of mass of the plume is best characterized by the laterally unconstrained plume speed and thickness. While there is some scatter due to the varying inflow temperature, the majority of the variability in the observed sedimentation extent is well characterized by the relatively simple analytical expression.

The laterally unconstrained analytical expression for sedimentation extent is also compared across all three sediment size classes used in the model scenarios (Table 1). Although the two smaller sediment size classes are well predicted with the expression, the largest sediment size class ($w_s = 2.2\times10^{-2}$ m s^{-1}) is not well predicted with the analytical expression. The larger sediment size class tends to deposit near the river mouth and is therefore more influenced by the river inflow and the near-field properties than by the inflow intrusion. Given the variability in the sediment extent across various sediment size classes, it is important to understand that the appropriate sedimentation extent expression depends on the time period over which sediment is in suspension relative to the timescale of plume development. If the time scale of sediment settling is less than the timescale for the inflow intrusion to develop, then the transport dynamics of that sediment size class will not be influenced by the inflow intrusion. The largest sediment size class (Figure 12) is not well approximated with the intrusion expression because it settles within 20 m of the river mouth. At

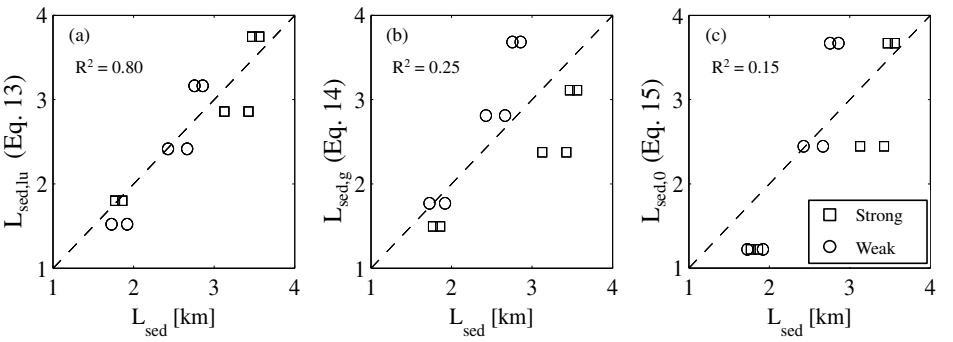

Figure 11. The extent of sedimentation, L_{sed} is compared to analytical expressions for the strong (squares) and weak (circles) stratification cases for the smallest sediment size class ($w_s = 1.4\times10^{-4}$ m s^{-1}) using (a) the laterally unconstrained intrusion properties (equation (13); $R^2 = 0.80$), (b) the geostrophic plume properties (equation (14); $R^2 = 0.25$), and (c) the inflow plume properties (equation (15); $R^2 = 0.15$).

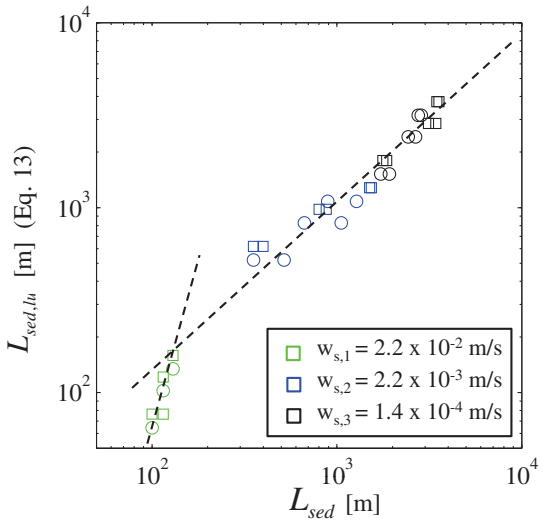

Figure 12. The sedimentation extent, L_{sed}, at which 50% of sediment has settled is compared to the analytical expression equation (13) for strong (squares) and weak (circles) stratification cases for all three sediment size classes on a log scale.

this distance from the river mouth, the plume has not yet intruded into the water column, therefore, it is not surprising that the intrusion-based sedimentation extent expression does not work well for the largest sediment size class. In fact, the sedimentation extent based on river inflow parameters performs the best for sediment transport of the largest size class.

Similarly, the length scale over which the plume transitions from laterally unconstrained to geostrophic will influence sediment transport. The plume speed changes along the length of the current from laterally unconstrained intrusion $u_{int,lu}$ to geostrophic intrusion $u_{int,g}$ as shown by the velocity vectors in Figure 13 for a characteristic scenario (Run 5) at the depth of the intrusion. If the sediment settles out of the intrusion before the plume reaches the southern boundary, the geostrophic estimate of sedimentation extent will be inappropriate. Because the sedimentation extent for the two smaller size classes is 1–4 km from the river mouth, the laterally unconstrained intrusion more accurately predicts the extent of sedimentation for the center of mass. However, the furthest extent of sedimentation for the smallest sediment size class (defined by the distance at which 95% of the sediment settles) was also compared to the analytical expressions. In this case, the extent of sedimentation ranges from 5–7 km from the river mouth and both the geostrophic and laterally unconstrained plume estimates perform similarly well ($R^2 = 0.77$ and 0.78, respectively). These results indicate that the transport of the smallest sediment size class at the furthest distance from the mouth is governed by both the laterally unconstrained plume dynamics as well as the geostrophic plume dynamics. As shown in Figure 13, sediment that propagates 6 km from the river mouth (dashed line) is partially transported by a laterally unconstrained intrusion and partially transported by the geostrophic intrusion. Therefore, it logically follows that both the laterally unconstrained and geostrophic intrusion expressions for sedimentation extent perform similarly well when considering the farthest extent of the smallest sediment size class. The effect of changing plume characteristics can be partially accounted for by accounting for the length scale over which the plume becomes a geostrophic boundary current. While the laterally unconstrained sedimentation extent performs best across the range of sediment size classes and scenarios considered, it is important to understand the plume dynamics and limitations of the sedimentation extent expressions.

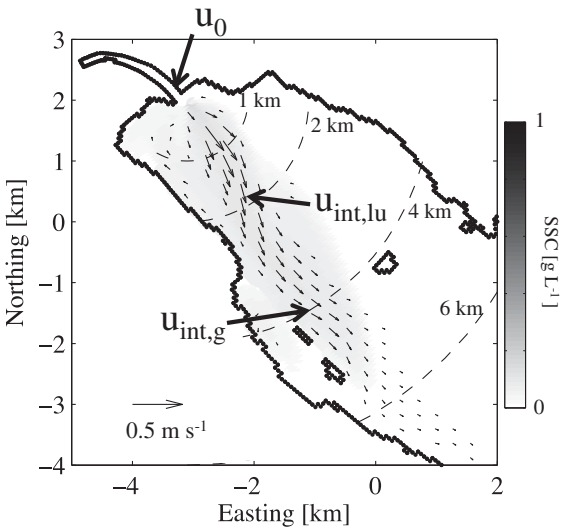

Figure 13. Velocity vectors and SSC are shown at the depth of the intrusion from Run 5 on day 2. The plume speed varies along the length of the plume as shown, where u_0 is the near-field inflow velocity, $u_{int,lu}$ is the laterally unconstrained intrusion velocity, and $u_{int,g}$ is the laterally constrained geostrophic plume speed. The dashed lines indicate distances from the river mouth.

We note that the simulation results do not include the effects of enhanced sediment settling through flocculation or convective sedimentation. These mechanisms have been observed to generate enhanced settling speeds (Davarpanah & Wells, 2016; Guo & He, 2011; Scheu et al., 2015), however, these effects are challenging to incorporate into a numerical model of a real system. The numerical model formulation does incorporate the densimetric effects of sediment such that when the density structure becomes unstable due to sediment settling, the MY2.5 vertical turbulence model will act to rapidly mix the unstable gradient resulting in slightly enhanced sedimentation rates. However, this will not likely accurately predict the enhanced sedimentation rates because the model is unable to explicitly resolve the small scale dynamics. The effects of enhanced sedimentation will be to reduce the sedimentation extent by modifying the sediment settling rate used in the analytical expression. Since the sedimentation extent varies proportionally to w_s, the overall formulation of the sedimentation extent expression in equation (13) should still be appropriate (i.e., $L_{sed} \sim Q^{2/3}$ and $N^{1/3}$), however, further research is needed to incorporate enhanced sedimentation effects. While there are

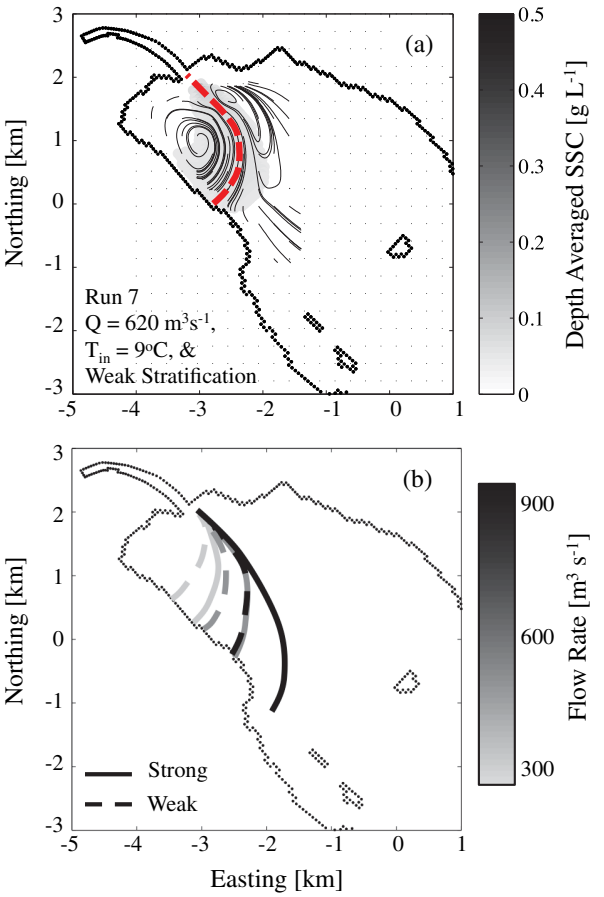

Figure 14. Depth-averaged SSC and streamlines at the depth of the intrusion (20 m) when the plume first impacts the southern boundary for Run 7 with the stagnation streamline indicated by the red dashed line (a). The stagnation streamlines are shown for all cool inflow temperature runs (Runs 1, 3, 5, 7, 9, and 11) with the volume flow rate (indicated by grayscale) and strong and weak stratification scenarios indicated by the solid and dashed lines, respectively (b). Red dashed line in (a) corresponds to dark gray dashed line in (b).

numerous observations and small scale studies that highlight the importance of these mechanisms for sediment transport (Davarpanah & Wells, 2016; Fox et al., 2004; Guo & He, 2011; Scheu et al., 2015; Shao et al., 2017), properly parameterizing the effects for a sediment transport model is an active area of research.

4.3. Rotational Trapping

While the simplified analytical expression for sedimentation extent works reasonably well, rotation can lead to trapping of material near the mouth, particularly for small flow rates. The recirculating region was highlighted in Figure 9b for the larger flow case (Run 8) in which a small amount of material is observed in a recirculating region near the mouth. To quantify the influence of rotation on the plume dynamics, we computed the location at which the plume first impacts the southern boundary. The location of impact was computed as the stagnation point of the streamline at the point in time when the plume first impacts the southern boundary at the depth of the intrusion. As an example, streamlines are shown in Figure 14a for Run 7 at the depth of the intrusion (approximately 20 m) at approximately 1 day into the simulation. The streamlines are computed using simulated velocities at the intrusion depth and originate from locations that are uniformly seeded throughout the domain. The streamlines show the stagnation streamline (the streamline that impacts the boundary indicated by the red dashed line in Figure 14a) and the presence of two recirculation regions, which are a common feature due to lateral shear in a jet-like plume. The beginning of the alongshore boundary current can also be seen in some of the streamlines that run parallel to the shore. At later times in the simulation, the alongshore boundary current becomes more dominant and the streamlines are predominantly oriented parallel to the southern boundary.

The stagnation streamlines were computed for all of the cooler inflow scenarios (Runs 1, 3, 5, 7, 9, and 11) and shown in Figure 14b. The distance from the river mouth at which the plume impinges on the boundary increases with the volume flow rate (indicated by the grayscale) and also increases with strength of the ambient stratification. For instance, the strong stratification cases (solid lines) propagate further into Pallanza Bay compared to the weaker stratified cases (dashed lines) given the same inflow rate. The distance that the plume propagates into the system (as characterized by the streamlines) is expected to scale with the radius of deformation based on the intrusion plume speed $L_R \approx (QN^2)^{1/3} f^{-1}$. This expression is consistent with our results because, as the intrusion velocity decreases (due to either decreasing volume flow or strength of stratification), the radius of deformation decreases, implying that the plume will be influenced by rotation over shorter length scales.

The intrusion radius of deformation provides an indication of the impact of rotation on the plume compared to a relevant length scale such as the width of Pallanza Bay. The ratio of the deformation radius to the basin width, B, was used by Pilotti et al. (2014) to understand the presence of a recirculating region in a laboratory model of an inflow intrusion into a rotational system. The ratio is defined as the basin Rossby number ($Ro = u_{int}(fB)^{-1}$) and is indicated in Table 4 for all simulated scenarios. For cases in which L_R is large compared to the width of the bay ($Ro > 1$), only a weak recirculating region develops. However, for cases in which L_R is small compared to the width of the bay ($Ro < 1$), the plume can become trapped in a recirculating bulge region near the river mouth. The radius of deformation provides an approximate metric for determining the appropriate sedimentation extent expression (laterally unconstrained or geostrophic) to use for prediction of the sedimentation extent.

While the recirculating region was observed in nearly all simulations, a significant portion of the plume is not rotationally trapped and propagates as a boundary current. For this reason, the simple expression for sedimentation extent works well because the extent is well estimated for a plume that is propagating away from the river mouth. However, as the recirculating region becomes more significant, we anticipate that a portion of the transport will be rotationally constrained such that the region of sedimentation will be confined by the radius of deformation (as shown in Wells, 2009 and Wells & Cossu, 2013). This implies that the sedimentation extent expression could be modified to incorporate the loss of mass in a recirculating region by appropriately reducing the volume flow rate in the sedimentation extent expression based on the volume of flow in the boundary current. The fraction of the inflow plume that is trapped in a recirculating region (versus transported in the boundary current) is expected to depend on the basin Rossby number. This effect was not fully investigated in the present manuscript but is instead left to an idealized modeling study with varying plume properties and basin widths (see Scheu et al. (2016)).

4.4. Counter-Clockwise Circulation

In addition to the anticyclonic recirculation region that trapped sediment near the river mouth, a cyclonic recirculation region also developed in all scenarios (see streamlines in Figure 15). Although the details and dynamics of this region are beyond the scope of this paper, it may be a mechanism for driving transport to the northern part of Pallanza Bay, potentially explaining how sediment from a river plume may settle to the left, rather than the right of a river mouth in the Northern hemisphere. Figure 15 shows velocity vectors at the depth of the inflow intrusion (30 m) on day 3 of the simulation (the falling end of the hydrograph) for three different flow scenarios. Also shown is the depth-averaged concentration of a passive scalar ($w_s = 0$) originating at the river boundary. A passive scalar was used to accentuate the effect of the counter-clockwise eddy, because the concentration is not reduced by settling. The cyclonic recirculating region is first observed near the river mouth (recall cyclonic streamlines from Figure 14a) and then propagates away from it as the flow rate increases with time. The recirculation region then persists in the same location throughout the duration of the simulation periods (10 days), decaying weakly in time and developing farther away from the river mouth for the larger inflows. While not included here, modeled scenarios with a constant flow rate produced similar results, indicating that the recirculation region is not driven by temporal variability of the hydrograph.

We believe that the relative steady distance of this recirculation region from the river mouth scales with the deformation radius of the intrusion because the region develops closer to the river mouth for the weakly stratified cases given the same inflow rate. In some cases, this cyclonic circulation region can drive sediment to the northern part of the bay. However, owing to settling, small amounts of sediment are transported to the northern portion of the bay and only when the recirculating region develops relatively close to the river mouth. This transport is consistent with observations of measured sedimentation from sediment traps at sites S5 and S6. While the details and dynamics of this region are beyond the scope of this paper, it may be a mechanism for driving transport to the northern boundary of Pallanza Bay, despite the persistent

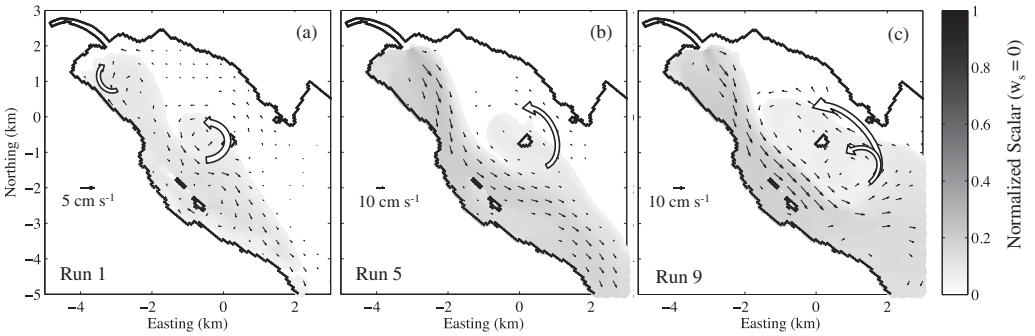

Figure 15. Snapshots on day 3 (after the inflow has peaked) of velocity vectors at the intrusion depth (30 m) and normalized scalar concentration (grayscale) for low (a), moderate (b), and high (c) inflow cases, corresponding to Runs 1, 5, and 9, respectively, with a warm inflow temperature of 11°C and strong stratification. Recirculation regions are indicated by the white arrows.

transport along the southern boundary by the primary intrusion plume. The recirculation region appears to be generated by lateral shear and is weakly damped, and persists through the duration of the scenarios.

This counter-clockwise recirculation region was also observed in laboratory experiments of inflow intrusions into a lab-scale model of Lake Iseo, Italy (Pilotti et al., 2014). In that study, the recirculation region persistently developed in cases with rotation and was more pronounced in cases with stratification, although the authors were unable to recreate the counter-clockwise recirculation in their numerical model. The counter-clockwise recirculation regions were also observed in laboratory studies of selective withdrawal from a stratified rotational system (Monismith & Maxworthy, 1989) and in coastal surface plume studies (Fong & Geyer, 2002; Horner-Devine et al., 2006), although the recirculating region typically propagates away from the coastal current and has a limited impact on sediment transport.

5. Summary and Conclusions

Inflow intrusions can drive sediment transport in a stratified lacustrine system and the extent of sediment transport in these systems can be an important indicator of the impact of introduced material on an ecosystem. Field observations and numerical modeling were conducted to investigate sediment transport and deposition from river inflow intrusions into a seasonally stratified lake influenced by rotation. Five inflow events were observed over nine months of field observations. The observed events occurred over a range of inflow and seasonal stratification conditions and were used to evaluate the numerical and sediment transport model performance. Overall, the model accurately reproduced the river plume dynamics and associated sediment deposition over five validation events with good to excellent skill scores. The model compared less favorably with observations when small changes in plume density in a weakly stratified system led to vertical movement of the plume through the water column. Enhanced sediment settling below the observed intrusion plumes was also not resolved in the model and is likely due to convective sedimentation or flocculation that is not captured by the model formulation because better methods are needed to parameterize these effects. However, in general, the good to excellent skill scores across all validation periods indicate that the model is correctly capturing the complex river inflow and intrusion dynamics. The sediment trap comparison also indicates that the model is correctly representing sediment transport dynamics in the mid- and far-field regions of the plume. The validated model was used to simulate a range of realistic scenarios to evaluate sediment transport and deposition from inflow intrusions.

The model scenarios were used to develop and evaluate a simple analytical expression for sedimentation extent in a real system based on an expression for sedimentation extent in surface plumes (Geyer et al., 2004) that was modified based on the thickness and speed of a laterally unconfined intrusion. The expression captures the trend in sedimentation extent utilizing only a priori knowledge of the flow rate and stratification. The expression based on the laterally unconstrained intrusion was a better estimate of sedimentation extent compared to the laterally bounded geostrophic plume for the sediment size classes and basin size considered. The expression for a geostrophic intrusion (equation (14)) was also evaluated and did not predict the transport dynamics as well as the laterally unconstrained intrusion estimate except in the case of the furthest extent of the smallest sediment size class. The timescale of sediment settling determines the relevant plume dynamics associated with transport and the expression should be applied carefully. The largest sediment size class settles in the immediate vicinity of the river mouth before the plume intrudes and the simple analytical expression based on the intrusion plume speed is not appropriate. Additionally, smaller sediment size classes that remain in suspension for longer periods of time may be more influenced by the geostrophic plume such that the sedimentation extent scales based on the geostrophic intrusion parameters rather than the laterally unconstrained intrusion parameters may be more reliable. Accurate characterization of the timescales of plume develop and sediment settling will be important to ensure the analytical expression is appropriately applied.

The simple expression for the sedimentation extent does not capture any lateral variability in the plume. Rotation drives the intrusive plumes toward the southern boundary and, in all cases considered, a boundary current formed along the southern boundary, and a small recirculating region formed near the river mouth that trapped sediment. The distance that the plume propagated before turning due to rotation (as characterized by the location where the plume impacts the southern boundary) generally scales with the deformation radius of the plume. The width of the bay however, acts to modify the plume trajectory such that the

amount of material trapped in a recirculating region for the same initial and inflow conditions will depend on the basin width. The extent of sediment transport in the recirculating region will be rotationally constrained such that the analytical transport expression derived in this manuscript will be inappropriate. However, assuming that some fraction of the plume propagates away from the river mouth as a boundary current, the expression could be modified to account for mass lost in the recirculating region (by appropriately modifying the flow rate in the intrusion, Q). Therefore, the expression of transport for an inflow intrusion should be applied carefully to ensure the appropriate plume dynamics are captured. Nonetheless, the simple expression performs well across the range of realistic scenarios observed in Pallanza Bay for the two smaller sediment size classes. Finally, a cyclonic circulation region was observed across all scenarios at a distance from the river mouth that increased with the magnitude of the inflow. We hypothesize that this may be a potential driver of sediment transport toward the northern boundary of the bay although more work is needed to characterize the dynamics of this region.

Acknowledgments
The authors would like to thank Diana Lin and Richard Luthy for providing data of sediment deposition from sediment traps during our hydrodynamic deployments and Alessandoro Oggioni (Consiglio Nazionale delle Ricerche) and Craig Jones (Integral Consulting Inc) for providing bathymetry data sets of Lake Maggiore. We would also like to thank Luca Ziliani (Environ, Italy), Daniele Bocchiola (personal communication. 2015, Politecnico di Milano), and Craig Jones (Integral Consulting, Inc.) for sharing their measurements of river flow rate and sediment load as well as for their insight regarding the study site. This work was made possible through a grant for Eni S.p.a. under research agreement number 4310016333 and we are grateful for the support of Eni and Syndial scientific officers Bibiana Groppelli, Pietro Cesti, Luciano Zaninetta, and Giorgio Bianchi. The fieldwork would not have been possible without the logistical support of Elisa Bizzoto (Environ), Federico Santoro (Environ), Massimo Magagnoli (Carma Coring), and Renato Brughera (Cantiere del Verbano). The authors would also like to thank Matthew Wells and two anonymous reviewers whose comments and suggestions helped improve and clarify this manuscript. All data used in this manuscript can be accessed on Zenodo: https://zenodo.org/record/1206188#.Ws6_LdPwYkg. Further details can be provided by the corresponding author upon request.

References

Alavian, V., Jirka, G. H., Denton, R. A., Johnson, M. C., & Stefan, H. G. (1992). Density currents entering lakes and reservoirs. *Journal of Hydraulic Engineering*, *118*(11), 1464–1489.
Allen, J. I., Holt, J. T., Blackford, J., & Proctor, R. (2007). Error quantification of a high-resolution coupled hydrodynamic ecosystem coastal-ocean model: Part 2. Chlorophyll-a nutrients and SPM. *Journal of Marine Systems*, *68*, 381–404.
Ambrosetti, W., & Barbanti, L. (1999). Deep water warming in lakes: An indicator of climatic change. *Journal of Limnology*, *58*, 1–9.
Benjamin, T. B. (1968). Gravity currents and related phenomena. *Journal of Fluid Mechanics*, *31*, 209–248.
Bertoni, R. (2007). Ricerche sell'evoluzione del Lago Maggiore. Aspetti limnologici., Programma quinquennale 2003 - 2007. Campagna 2007 e Rapporto quinquennale 2003–2007., *Commissione Internazionale per la protezione delle acque italo-svizzere (CIPAIS)*.
Bertoni, R. (2009). Ricerche sell'evoluzione del Lago Maggiore. Aspetti limnologici., Campagna 2009, *Commissione Internazionale per la protezione delle acque italo-svizzere (CIPAIS)*, pp. 1–31.
Bolster, D., Hang, A., & Linden, P. F. (2008). The front speed of intrusions into a continuously stratified medium. *Journal of Fluid Mechanics*, *594*, 369–377.
Canuto, V. M., Howard, A., Cheng, Y., & Dubovikov, M. S. (2001). Ocean turbulence I: One–point closure model — Momentum and heat vertical diffusivities. *Journal of Physical Oceanography*, *31*, 1413–1426.
Cenedese, C., & Adduce, C. (2010). A new parameterization for entrainment in overflows. *Journal of Physical Oceanography*, *40*(8), 1835–1850.
Chikita, K. (1990). Sedimentation by river-induced currents: Field measurements and interpretation. *Sedimentology*, *37*, 891–905.
Chua, V. P., & Fringer, O. B. (2011). Sensitivity analysis of three-dimensional salinity simulations in North San Francisco Bay using the unstructured-grid SUNTANS model. *Ocean Modelling*, *39*, 332–350.
Chung, S. W., Hipsey, M. R., & Imberger, J. (2009). Modelling the propagation of turbid density inflows into a stratified lake: Daecheong Reservoir, Korea. *Environmental Modelling & Software*, *24*, 1467–1482.
Cortés, A., Fleenor, W. E., Wells, M. G., de Vicente, I., & Rueda, F. J. (2014). Pathways of river water to surface layers of stratified reservoirs. *Limnology and Oceanography Methods*, *59*(1), 233–250.
Davarpanah, J., & Wells, M. G. (2016). Enhanced sedimentation beneath particle-laden flows in lakes and the ocean due to double-diffusive convection. *Geophysical Research Letters*, *43*, https://doi.org/10.1002/2016GL069547
El-Gawad, S. A., Cantelli, A., Pirmez, C., Minisin, D., Sylvester, Z., & Imran, J. (2012). Three-dimensional numerical simulation of turbidity currents in a submarine channel on the seafloor of the Niger Delta slope. *Journal of Geophysical Research*, *117*, C05026. https://doi.org/10.1029/2011JC007538
Ellison, T. H., & Turner, J. S. (1959). Turbulent entrainment in stratified flows. *Journal of Fluid Mechanics*, *6*(3), 423–448.
Fischer, H. B., List, E. J., Koh, R. C. Y., Imberger, J., & Brooks, N. H. (1979). *Mixing in inland and coastal waters*. New York, NY: Academic Press.
Fischer, H. B., & Smith, R. D. (1983). Observations of transport to surface waters from a plunging inflow to Lake Mead. *Limnology and Oceanography*, *28*(2), 258–272.
Flower, R. J. (1991). Field calibration and performance of sediment traps in a eutrophic holomictic lake. *Journal of Paleolimnology*, *5*, 175–188.
Fong, D. A., & Geyer, W. R. (2002). The alongshore transport of freshwater in a surface-trapped river plume. *Journal of Physical Oceanography*, *32*, 957–972.
Ford, D. E., & Johnson, M. C. (1983). *An assessment of reservoir density currents and inflow processes* (Tech. rep. E-83-7, DTIC Document). Vicksburg, MS: Ford, Thornton, Norton, and Associated, Ltd.
Fox, J. M., Hill, P. S., Milligan, T. G., & Boldrin, A. (2004). Flocculation and sedimentation on the Po River Delta. *Marine Geology*, *203*(1–2), 95–107.
Fringer, O. B., Gerritsen, M., & Street, R. L. (2006). An unstructured-grid, finite-volume, nonhydrostatic, parallel coastal ocean simulator. *Ocean Modelling*, *14*(3–4), 139– 173.
Fringer, O. B., & Street, R. L. (2003). The dynamics of breaking progressive interfacial waves. *Journal of Fluid Mechanics*, *494*, 319–353.
Gartner, J. W. (2004). Estimating suspended solids concentrations from backscatter intensity measured by acoustic Doppler current profiler in San Francisco Bay, California. *Marine Geology*, *211*, 169–187.
Geyer, W. R., Hill, P. S., & Kineke, G. C. (2004). The transport, transformation and dispersal of sediment by buoyant coastal flows. *Continental Shelf Research*, *24*, 927–949.
Guo, L., & He, Q. (2011). Freshwater flocculation of suspended sediments in the Yangtze River, China. *Ocean Dynamics*, *61*, 371–386.
Hanggi, D., & Carr, P. W. (1985). Errors in exponentially modified Gaussian equations in literature. *Analytical Chemistry 57*(12), 2394–2395.
Hill, P. S., Milligan, T. G., & Geyer, W. R. (2000). Controls on effective settling velocity of suspended sediment in the Eel River flood plume. *Continental Shelf Research*, *20*(16), 2095–2111.
Horner-Devine, A. R., Fong, D. A., Monismith, S. G., & Maxworthy, T. (2006). Laboratory experiments simulating a coastal river inflow. *Journal of Fluid Mechanics*, *555*, 203–232.

Imberger, J., & Hamblin, P. F. (1982). Dynamics of lakes, reservoirs, and cooling ponds. *Annual Review of Fluid Mechanics*, *14*, 153–187.
Imberger, J., & Patterson, J. C. (1990). Physical limnology, *Advances in Applied Mechanics*, *27*, 305–475.
Jones, C. (2012). *Idrodinamica e trasporto dei sedimenti nella Baia di Pallanza* (Technical report). Santa Cruz, CA: Sea Engineering (for ENVIRON Italy).
Killworth, P. D., & Carmack, E. C. (1979). A filling-box model of river-dominated lakes. *Limnology and Oceanography*, *24*(2), 201–217.
Kozerski, H.-P. (1994). Possibilities and limitations of sediment traps to measure sedimentation and resuspension. *Hydrobiologia*, *284*, 93–100.
Laborde, S., Antenucci, J. P., Copetti, D., & Imberger, J. (2010). Inflow intrusions at multiple scales in a large temperate lake. *Limnology and Oceanography*, *55*, 1301–1312.
Lan, K., & Jorgenson, J. W. (2001). A hybrid of exponential and gaussian functions as a simple model of asymmetric chromatographic peaks. *Journal of Chromatography A*, *915*, 1–13.
Large, W. G., & Pond, S. (1981). Open ocean momentum flux measurements in moderate to strong winds. *Journal of Physical Oceanography*, *11*, 324–336.
Lien, J.-M., Liu, G., & Langevin, C. D. (2015). GRIDGEN version 1.0 - A computer program for generating unstructured finite-volume grids, *U.S. Geological Survey Open-File Report 2014–1109*, 26 p.
Lin, D. (2015). *Field and laboratory assessment of natural and engineered attenuation processes of DDT-impacted sediment with an emphasis on bioturbation effect* (Ph.D. thesis). Stanford, CA: Stanford University.
Lin, D., Cho, Y.-M., Oen, A., Eek, E., Tommerdahl, J. P., & Luthy, R. G. (2017). Toolset for assessment of natural recovery from legacy contaminated sediment: Case study of Pallanza Bay, Lake Maggiore, Italy. *Water Research*, *121*, 109–119.
Marco, V. B. D., & Bombi, G. G. (2001). Mathematical functions for the representation of chromatographic peaks. *Journal of Chromatography A*, *931*, 1–30.
Marechal, D. (2004). *A soil-based approach to rainfall-runoff modelling in ungauged catchments for England and Wales* (Ph.D. thesis). Cranfield, England: Cranfield University.
Maxworthy, T., Leilich, J., Simpson, J. E., & Meiburg, E. H. (2002). The propagation of a gravity current into a linearly stratified fluid. *Journal of Fluid Mechanics*, *453*, 371–394.
Mellor, G. L., & Yamada, T. (1982). Development of a turbulence closure model for geophysical fluid problems. *Review of Geophysics*, *20*, 851–875.
Millero, F. J., Chen, C.-T., Bradshaw, A., & Schleider, K. (1980). A new high pressure equation of state for seawater. *Deep Sea Research Part A. Oceanographic Research Papers*, *27*(3–4), 225–265.
Millero, F. J., & Poisson, A. (1981). International one-atmosphere equation of state of seawater. *Deep Sea Research Part A. Oceanographic Research Papers*, *28*(6), 625–629.
Monismith, S. G., & Maxworthy, T. (1989). Selective withdrawal and spin-up of a rotating stratified fluid. *Journal of Fluid Mechanics*, *199*, 377–401.
Morillo, S., Imberger, J., Antenucci, J. P., & Woods, P. F. (2008). Influence of wind and lake morphometry on the interaction between two rivers entering a stratified lake. *Journal of Hydraulic Engineering*, *134*(11), 1579–1589.
Murphy, A. H., & Epstein, E. S. (1989). Skill scores and correlation coefficients in model verification. *Monthly Weather Review*, *117*, 572–585.
Nash, J. E., & Sutcliffe, J. V. (1970). River flow forecasting through conceptual models. Part I - A discussion of principles. *Journal of Hydrology*, *10*(3), 282–290.
Nof, D., & Gorder, S. V. (1988). The propagation of gravity currents along contintental shelves. *Journal of Physical Oceanography*, *18*, 481–491.
Pilotti, M., Valeria, G., Gregorini, L., Milanesi, L., & Hogg, C. A. R. (2014). Study of tributary inflows in Lake Iseo with a rotating physical model. *Journal of Limnology*, *73*(1), 131–145.
Pimenta, F. M., Kirwan Jr, A. D., & Huq, P. (2011). On the transport of buoyant coastal plumes. *Journal of Physical Oceanography*, *41*, 620–640.
Rayson, M. D., Gross, E. S., & Fringer, O. B. (2015). Modeling the tidal and sub-tidal hydrodynamics in a shallow, micro-tidal estuary. *Ocean Modelling*, *89*, 29–44.
Rueda, F., & Schladow, G. (2003). Dynamics of a large polymictic lake. II: Numerical simulations. *Journal of Hydraulic Engineering*, *129*(2), 92–101.
Rueda, F. J., & MacIntyre, S. (2010). Modelling the fate and transport of negatively buoyant storm-river water in small multi-basin lakes. *Environmental Modelling & Software*, *25*, 146–157.
Scheu, K. R., Fong, D. A., Monismith, S. G., & Fringer, O. B. (2015). Sediment transport dynamics near a river inflow in a large alpine lake. *Limnology and Oceanography*, *60*, 1195–1211.
Scheu, K. R., Fong, D. A., Monismith, S. G., & Fringer, O. B. (2016). *Sediment transport due to river plumes in stratified, rotationally-influenced lakes* (Ph.D. thesis). Stanford, CA: Stanford University.
Shao, Y.-C., Hung, C.-Y., & Chou, Y.-J. (2017). Numerical study of convective sedimentation through a sharp density interface. *Journal of Fluid Mechanics*, *824*, 513–549.
Shimizu, K., Imberger, J., & Kumagai, M. (2007). Horizontal structure and excitation of primary motions in a strongly stratified lake. *Limnology and Oceanography*, *56*, 2641–2655.
Stokes, G. G. (1851). On the effect of the internal friction of fluids on the motion of pendulums, *Transactions of the Cambridge Philosophical Society*, *IX*, 8.
Turner, J. S. (1986). Turbulent entrainment: The development of the entrainment assumption, and its application to geophysical flows. *Journal of Fluid Mechanics*, *173*, 431–471.
Wall, G. R., Nystrom, E. A., & Litten, S. (2006). Use of an ADCP to compute suspended sediment discharge in the Tidal Hudson River, Ney York (U.S. Geological Survey Scientific Investigations Report 2006-5055, pp. 1–14). New York, NY: U.S. Geological Survey.
Wang, B., Giddings, S. N., Fringer, O., Gross, E., Fong, D. A., & Monismith, S. G. (2011). Modeling and understanding turbulent mixing in a macrotidal salt wedge estuary. *Journal of Geophysical Research*, *116*, C02036. https://doi.org/110.1029/2010JC006135
Wells, M., Cenedese, C., & Caulfield, C. P. (2010). The relationship between flux coefficient and entrainment ratio in density currents. *Journal of Physical Oceanography*, *40*, 2713–2727.
Wells, M., & Cossu, R. (2013). The possible role of Coriolis forces in structuring large-scale sinuous patterns of submarine channel-levee systems. *Philosphical Transactions of Royal Society A*, *371*(2004),
Wells, M., & Nadarajah, P. (2009). The intrusion depth of density currents flowing into stratified water bodies. *Journal of Physical Oceanography*, *39*(8), 1935–1947.
Wells, M. G. (2009). How Coriolis forces can limit the spatial extent of sediment deposition of a large-scale turbidity current. *Sedimentary Geology*, *218*, 1–5.